



**HAL**  
open science

# Significant wave heights from Sentinel-1 SAR: Validation and applications

J. E. Stopa, A. Mouche

► **To cite this version:**

J. E. Stopa, A. Mouche. Significant wave heights from Sentinel-1 SAR: Validation and applications. Journal of Geophysical Research. Oceans, 2017, 122, pp.1827-1848. 10.1002/2016JC012364. insu-03682753

**HAL Id: insu-03682753**

**<https://insu.hal.science/insu-03682753>**

Submitted on 22 Jun 2022

**HAL** is a multi-disciplinary open access archive for the deposit and dissemination of scientific research documents, whether they are published or not. The documents may come from teaching and research institutions in France or abroad, or from public or private research centers.

L'archive ouverte pluridisciplinaire **HAL**, est destinée au dépôt et à la diffusion de documents scientifiques de niveau recherche, publiés ou non, émanant des établissements d'enseignement et de recherche français ou étrangers, des laboratoires publics ou privés.

Copyright

## RESEARCH ARTICLE

10.1002/2016JC012364

## Significant wave heights from Sentinel-1 SAR: Validation and applications

J. E. Stopa <sup>1</sup> and A. Mouche<sup>1,2</sup><sup>1</sup>Laboratoire d'Océanographie Physique et Spatiale (LOPS), IUEM, University of Brest, CNRS, IRD, Ifremer, Brest, France,<sup>2</sup>School of Marine Sciences, Nanjing University of Information Science and Technology, Nanjing, China

## Key Points:

- Wave parameters are retrieved empirically from S1A SAR using two approaches
- Neural networks are trained using wave data from models and verified with measurements
- SAR wave heights complement existing sources and are reliable under a large range of environmental conditions

## Supporting Information:

- Supporting Information S1
- Table S1
- Table S2
- Table S3
- Table S4

## Correspondence to:

J. E. Stopa,  
justin.stopa@ifremer.fr

## Citation:

Stopa, J. E., and A. Mouche (2017), Significant wave heights from Sentinel-1 SAR: Validation and applications, *J. Geophys. Res. Oceans*, 122, 1827–1848, doi:10.1002/2016JC012364.

Received 24 SEP 2016

Accepted 14 DEC 2016

Accepted article online 26 DEC 2016

Published online 10 MAR 2017

**Abstract** Two empirical algorithms are developed for wave mode images measured from the synthetic aperture radar aboard Sentinel-1 A. The first method, called CWAVE\_S1A, is an extension of previous efforts developed for ERS2 and the second method, called  $F_{nn}$ , uses the azimuth cutoff among other parameters to estimate significant wave heights ( $H_s$ ) and average wave periods without using a modulation transfer function. Neural networks are trained using colocated data generated from WAVEWATCH III and independently verified with data from altimeters and in situ buoys. We use neural networks to relate the nonlinear relationships between the input SAR image parameters and output geophysical wave parameters. CWAVE\_S1A performs well and has reduced precision compared to  $F_{nn}$  with  $H_s$  root mean square errors within 0.5 and 0.6 m, respectively. The developed neural networks extend the SAR's ability to retrieve useful wave information under a large range of environmental conditions including extratropical and tropical cyclones in which  $H_s$  estimation is traditionally challenging.

## 1. Introduction

Since the launch of Seasat in 1978, it has been known that synthetic aperture radar (SAR) can measure two-dimensional (2-D) (wavenumber-direction) wave spectra from space. Two-dimensional wave spectra estimated from spaceborne SAR have important applications in research and have aided in the improvement of numerical models. For example SAR 2-D wave spectra improved global forecast models using assimilation [Aouf and Lefevre, 2015], improved wave model performance [Ardhuin et al., 2010; Stopa et al., 2015a], enabled study of swell evolution [Collard et al., 2009; Ardhuin et al., 2009; Stopa et al., 2016], and enabled study of crossing seas [Li, 2016]. The imaging mechanisms in SAR over the ocean surface include tilt modulation, hydrodynamic modulation, and velocity bunching which is a nonlinear distortion [Alpers et al., 1981; Hasselmann et al., 1985]. There has been significant efforts in understanding the image to wave spectrum transformation [Alpers et al., 1981; Hasselmann et al., 1985; Hasselmann and Hasselmann, 1991; Krogstad et al., 1994; Engen and Johnsen, 1995]. Wave spectra are estimated using two approaches. The first uses the full nonlinear inversion and requires external information often taken from numerical wave models to estimate a full wave spectrum [Hasselmann et al., 1996; Schulz-Stellenfleth, 2005]. The second method uses the quasi-linear inversion and does not need ancillary wave information, but produces a wave spectrum that cannot fully resolve high-frequency waves [Chapron et al., 2001; Collard et al., 2005]. Therefore, 2-D wave spectra from SAR cannot be used to independently estimate integral wave parameters such as the significant wave height ( $H_s$ ), the most widely used sea state parameter. This limits the applications of the SAR data.

Velocity bunching causes a distortion along the motion of the satellite called the azimuth cutoff. This quantity is effectively a minimum observable wavelength that the SAR can image under the given sea state [Kerbaol et al., 1998] and is proportional to the total variance of the orbital wave velocity [Stopa et al., 2015b]. Consequently in high sea states common to extratropical and tropical storms when the cutoff is large (e.g., >450 m), the majority of the wave spectral components will be unreliable. In Figure 1 we illustrate this effect with example ocean wave signatures in Sentinel-1 A (S1A) sea surface roughness images. In the left plot, there is a uniform backscatter with swell clearly visible and is aligned from the lower left to upper right consistent with the image spectrum (bottom left plot). In the middle plot, the cutoff is strong and the image appears blurred. The resulting image spectrum cannot resolve wavelengths below 431 m and the energy is

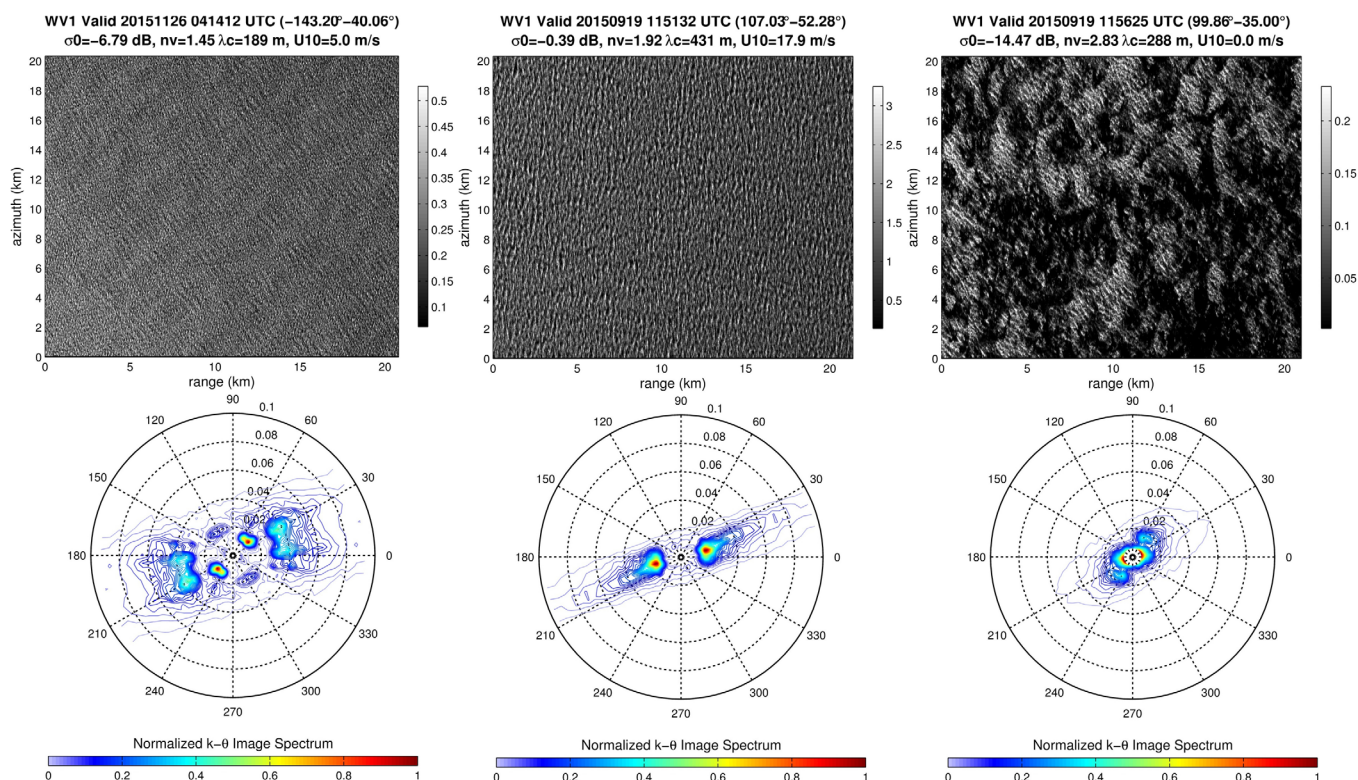


**Figure 1.** (top) S1A sea surface roughness (dB) and (bottom) normalized image spectra for (left) WV1 with small distortion, (middle) large distortion, and (right) poorly contrasted. The value for  $\sigma_0$  represents the normalized radar cross section see text for other variable definitions.

distorted into the range direction. In the right plot, we demonstrate a poorly contrasted ocean scene where the SAR imaging of waves is distorted by atmospheric effects and will make the inversion difficult.

Instead of using an image-to-wave inversion scheme, alternative approaches were developed to empirically estimate integral wave parameters from SAR ocean scenes. *Schulz-Stellenfleth et al.* [2007] were the first to develop a technique to derive wave parameters without explicit retrieval of wave spectra for the ERS2 mission (1996–1999), called CWAVE\_ERS. Following their approach, *Li et al.* [2011] developed CWAVE\_ENV for ENVISAT (2003–2012). *Romeiser et al.* [2015] use a similar method to estimate wave parameters with data from RADARSAT in tropical cyclones where observations are sparse and the extreme wind and wave conditions coupled with atmospheric features make the nonlinear SAR mapping challenging. In this paper, we extend these previous efforts to estimate integrated wave parameters for the recently launched Sentinel missions: S1A in April 2014 and S1B in May 2016. Integrated wave parameters will bring additional information with respect to the existing ocean swell parameters already included in the European Space Agency (ESA) Level-2 (L2) product. In addition, this will allow wave information to be retrieved from a broader range of sea states including storm conditions when the azimuth cutoff is large.

In this study, we develop empirical functions that estimate the  $H_s$  from SAR image parameters. We require that our algorithms rely only on SAR data without any ancillary information, remain computationally efficient, and adopt compact notation. We take two approaches. In the first, we extend the framework of *Schulz-Stellenfleth et al.* [2007] and we decompose the SAR image spectra into a set of 20 orthogonal components, which describe the shape of the SAR image spectrum and contain information about integral wave parameters [*Alpers et al.*, 1981; *Hasselmann and Hasselmann*, 1991]. In the second approach, we exploit the azimuth cutoff among other parameters to measure the sea state, since this parameter is dependent on the near surface wind speed ( $U_{10}$ ) and wave conditions [*Beal et al.*, 1983; *Vachon et al.*, 1994; *Kerbaol et al.*, 1998]. The azimuth cutoff estimated from ENVISAT shows a strong dependence between  $U_{10}$  and  $H_s$  at buoy collocations [*Stopa et al.*, 2015b]. Furthermore *Bruck and Lehner* [2015] and *Grieco et al.* [2016] show the parameter can be used to estimate  $H_s$  for TeraSARX and S1A, respectively. In this method, we use less input parameters than CWAVE and the input parameters are included by a systematic inclusion of each. We

use neural networks, which are an efficient machine learning technique, to describe the nonlinear relationships between our SAR input parameters and output geophysical parameters. Our approach is analogous to the well-developed techniques used for scatterometers which relate ocean wind vectors to measured sea surface roughness (called geophysical model functions, GMFs) [Stoffelen and Anderson, 1997; Mouche and Chapron, 2015].

The paper is organized as follows. We describe our data sources in section 2, including subsections dedicated to S1A, numerically derived wave data from WAVEWATCH III, and observations from altimeters and buoys. In section 3, we describe our model to retrieve ocean wave parameters from SAR. In section 4, we provide an independent verification with observations and demonstrate the added benefit of being able to estimate reliable significant wave heights from SAR. Our discussion and conclusions are given in sections 5 and 6, respectively.

## 2. Data Sources

This study uses wave data from satellites, buoys, and the spectral wave model WAVEWATCH III (hereinafter WW3). To train the GMFs, we use a colocated data set of approximately 500,000 S1A SAR images matched with wave spectra generated from WW3. To independently verify the developed functions we use observations from altimeters and buoys. All data sets are described in the following.

### 2.1. Sentinel-1 A Wave Mode

Sentinel-1 A was launched in April 2014 and is the first satellite equipped with a SAR in the ESA Sentinel constellation. For this study, we use data acquired in “wave mode” which has a nominal spatial resolution of 4 m with an approximate satellite footprint of  $20 \times 20$  km (see Figure 1). S1A operates in the C-Band at two incidence angles of  $23^\circ$  (WV1) and  $36^\circ$  (WV2) and an acquisition is made every 100 km along the orbit. S1A alternates between WV1 and WV2 along its track and vignettes with the same incidence angle are separated by 200 km. The sensor has the ability to acquire data for both VV (default) and HH polarization. S1A went into routine wave mode acquisition starting in July 2015. Accordingly, our results are based on data acquired from July 2015 to July 2016. There are roughly 260,000 images for both WV1 and WV2. It should be mentioned that all the results presented in this paper have been obtained using ESA Wave Mode L2 products acquired in VV polarization. Indeed, parameters such as  $\sigma_0$ , azimuth cutoff, incidence angle, image skewness, image kurtosis, and the 2-D image spectrum are included in the ESA L2 product.

SAR image processing relies on the backscattered signal phase analysis assuming a homogeneous and immobile surface to achieve high resolution. Over the ocean, scatterers with high-frequency displacements cannot be properly resolved by the SAR imaging mechanism. This leads to a cutoff value where waves with higher frequencies than the cutoff cannot be retrieved. Accordingly, the imaged SAR ocean scene is shifted proportionally to the orbital wave velocity which is related to the sea state ( $U_{10}$  and  $H_s$ ) [Kerbaol *et al.*, 1998; Stopa *et al.*, 2015b]. The effect is illustrated in Figure 1 (middle plot). Using linear wave theory the azimuth cutoff,  $(\lambda_c)$  in m can be written

$$\lambda_c = \pi \frac{R}{V} \sqrt{\int_0^\infty \omega^2 F(f) df} \tag{1}$$

where  $R$  is the range of the satellite to target calculated using the platform altitude of 713 km and incident angle  $\theta$  as  $\sin(\theta)$ ,  $V$  is the satellite velocity of 7570 m/s,  $\omega = 2\pi f$ ,  $f$  is the wave frequency, and  $F$  is the wave spectrum. Three different SAR scenes collected during the integration dwell-time are used to calculate cross spectra to reduce the speckle noise [Engen and Johnsen, 1995]. The real component of the average cross spectra in the azimuth direction is used to estimate the azimuth cutoff by minimizing the residuals between a Gaussian function. The azimuth cutoff is then approximated as

$$\lambda_c = \sqrt{2\pi} \sigma \tag{2}$$

where  $\sigma$  is the standard deviation of the Gaussian fit.

The normalized radar cross-section  $\sigma_0$  is an important parameter that is typically related to wind speed and direction [Quilfen *et al.*, 1999; Mouche and Chapron, 2015]. The normalized radar cross section,  $\sigma_0$  (in dB), is

calculated from the original digital number (DN) from the L1 product by using a look up table (*sigma-Nought*) which includes the absolute calibrated constant

$$\sigma_0 = |DN|^2 / \text{sigmaNought}^2. \quad (3)$$

In addition, the normalized variance from the image intensity,  $\langle I \rangle$

$$nv = \text{var} \left( \frac{I - \langle I \rangle}{\langle I \rangle} \right) \quad (4)$$

gives information regarding the image homogeneity as well as sea state. Both of these parameters calculated from the SAR images are important in deriving the integrated wave parameters [Schulz-Stellenfleth *et al.*, 2007; Li *et al.*, 2011].

## 2.2. WAVEWATCH III

The success of developing robust empirical algorithms depends on the accuracy and the range of environmental conditions we can associate to observations. Therefore to maximize the number of colocations, we use data generated by WW3. Spectral wave models have improved their accuracy by the development of the physical source term parameterizations [Ardhuin *et al.*, 2010; Stopa *et al.*, 2015a]. Our model implementation uses a 0.5° global grid with 24 directions and 32 frequencies ranging 0.0373–0.7159 Hz exponentially spaced with an increment of 1.1. WW3 is driven by 3 hourly winds and ice concentrations from the operational ECMWF product at 0.125° and uses the physical parameterizations of Raschle and Ardhuin [2013]. Frequency-direction wave spectra are collocated by linearly interpolating the model in time and using the closest point in space to match the S1A acquisitions. Co-located S1A/WW3 wave spectra from July 2015 to July 2016 are used to train the GMFs and cover the majority of the global ocean as observed in Figure 2. The top plot of Figure 2 shows the data density in 2° bins for WV1 with 260,000+ colocations and is approximately the same for WV2.

## 2.3. Observations: Altimeters and Buoys

Observations from both satellite altimeters and in situ buoys are used as independent data sources to compare the derived wave parameters from our models. The altimeter data set is composed of three missions: CRYOSAT, JASON2, and SARAL and have been quality controlled and corrected using in situ buoys by Queffelec and Croize-Fillon [2016] and [Sepulveda *et al.*, 2015]. Approximately 16,000 colocations are found using 100 km and 2 h as spatial and temporal constraints for both WV1 and WV2 with approximately 10 observations per 3° bin for July–December 2015 (see Figure 2). Buoy colocations are limited to 1 h and 100 km from NOAA Nation Data buoy center (NDBC), the Canadian Marine Environmental Data Service (MEDS), and the Coastal Data Information Program (CDIP) networks. Wave frequency spectra from 0.385 to 0.5 Hz are used to calculate integral wave parameters that were created by a 30 min average. There were 347 colocations found for WV1 and 225 colocations for WV2 and are mostly situated in the Northern Hemisphere (see Figure 2).

## 3. SAR Sea State Models

In the following subsections, we describe our training approach and define our input parameters for both algorithms: (1) CWAVE\_S1A which follows Schulz-Stellenfleth *et al.* [2007] orthogonal decomposition and (2)  $F_{nn}$  which relies on the azimuth cutoff.

### 3.1. Training Using Neural Networks

Neural networks are a convenient and versatile method to predict an outcome. We train our functions using a multi-layer perceptron (MLP) with backward propagation of errors [Hagan *et al.*, 2014]. This technique was used to derive wind speeds for altimeters [Gourrion *et al.*, 2002] and relate ocean surface wind vectors to SAR normalized radar cross section and geophysical Doppler centroid anomalies [Mouche and Chapron, 2015; Mouche *et al.*, 2012]. The advantage of the MLP is a relatively compact solution and fast computational speed. Thus, the number of coefficients is reduced compared to Schulz-Stellenfleth *et al.* [2007] and Li *et al.* [2011] who used linear regression with the possibility of having 625 different coefficients for CWAVE\_ERS

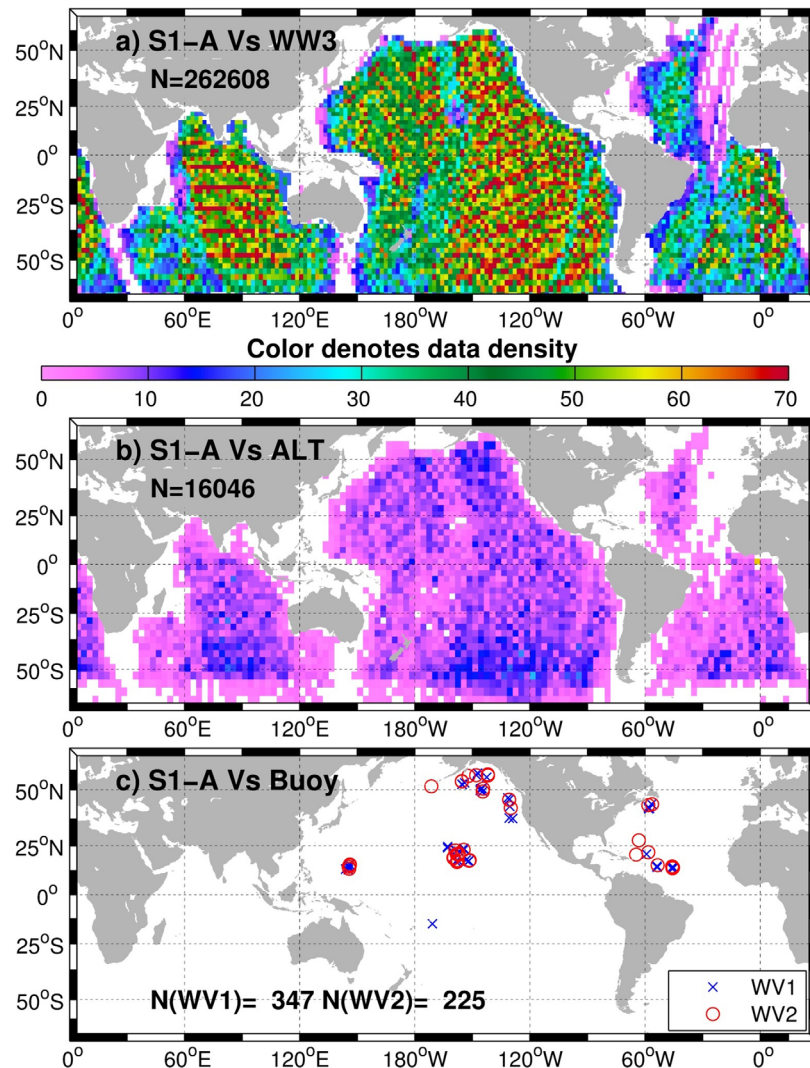


**Figure 2.** Collocated S1-A data with WW3 given in data density for  $2^\circ$  bins with (top) WV1 July 2015 to July 2016, altimeters including CRY-OSAT, JASON2, and SARAL given in data density for  $3^\circ$  bins with (middle) WV1 July 2015 to December 2016, and buoys locations for WV1 and WV2 from July 2015 to July 2016.

and CWAVE\_ENV making it nearly impossible for other researchers to replicate their results. Our networks consist of three layer MLP with an input layer, one hidden layer, and an output layer. A more detailed description is included in Appendix A. The number of neurons in the hidden layers is varied until an optimal solution is found, this is described in more detail for both CWAVE\_S1A and  $F_{nn}$ .

The MLP network is not trained in the traditional manner of dividing the data set into two subsections for training and independent testing and validation. This is due to the fact there is a relatively sparse distribution of the data at the extreme sea states as shown in the probability distributions in the top plots of Figure 3 for the collocated S1A/WW3 data set. This data set excludes the collocations between S1A/buoy and S1A/altimeter. We also discard the month of September 2015 in the training because we use it for independent verification. Notice there is a 47% chance of having a 2 m wave height and 13% chance of having a 7 m/s wind speed compared to other sea states. If we used this entire data set for training, the large differences in data density would lead to solutions that are biased towards higher density regions and result in poorly functioning GMFs [Hagan et al., 2014].

Therefore, we partition the data into 0.25 m/s bins for  $U_{10}$  and 0.5 m bins for  $H_s$  from 0 to 30 m/s and 0 to 15 m, respectively. We select 100 random samples from the equally spaced  $U_{10}$  bins and then further equalize across  $H_s$  bins. If a  $U_{10}$  bin contains fewer than 100 samples, all points are included. We reverse

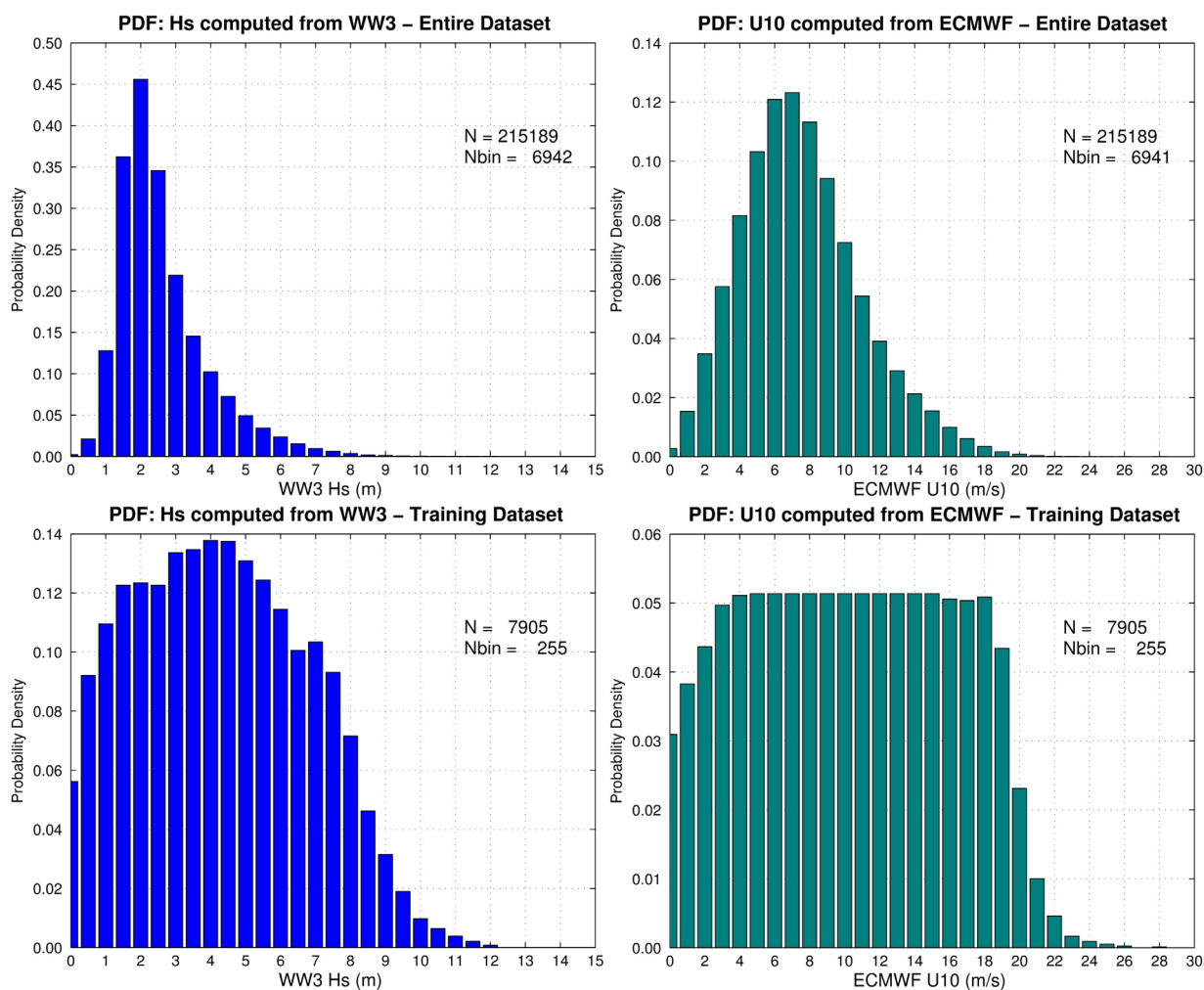


**Figure 3.** Probability density functions of (left)  $H_s$  and (right) U10 colocated S1-A data with (top) WW3 for WV1 July 2015 to July 2016 and (bottom) subset used in training excluding matchups between S1A/buoy and S1A/altimeter. The  $H_s$  data uses a 0.5 m bin and the U10 data has a 1 m/s bin.

the order by first subsampling with  $H_s$  and then U10 but the resulting functions had nearly identical performance. This subsample is only 3.5% of the entire WW3 training data set. Another benefit of the data reduction is an decrease of the computational time to train the GMFs. We repeated the same procedure to create the validation data set used in the MLP back propagation routine and implement the Levenberg-Marquardt algorithm to train the models. During training we assess the performance of the developed neural network using the mean square error (*mse*) for the GMF output  $x_m$  and the independent known output in the validation data set  $x_v$  for  $n$  points

$$mse = \frac{1}{n} \sum_{i=1}^n (x_{mi} - x_{vi})^2. \quad (5)$$

### 3.2. Filtering

SAR captures all ocean features including slicks, atmospheric gravity waves, and sea ice which contaminate the computation of wave parameters if not removed. In addition, if the image has low backscatter and is poorly contrasted like in right plot of Figure 1, wave features are difficult to resolve. We remove data with the following criteria:

1. We use data within the latitudes  $\pm 60^\circ$  to avoid sea ice, 7% of original data set
2. We ensure homogeneity by limiting the normalized variance  $1 \leq nv \leq 2$  for WV1 and  $1 \leq nv \leq 1.4$  for WV2, 1.98% of original data set.

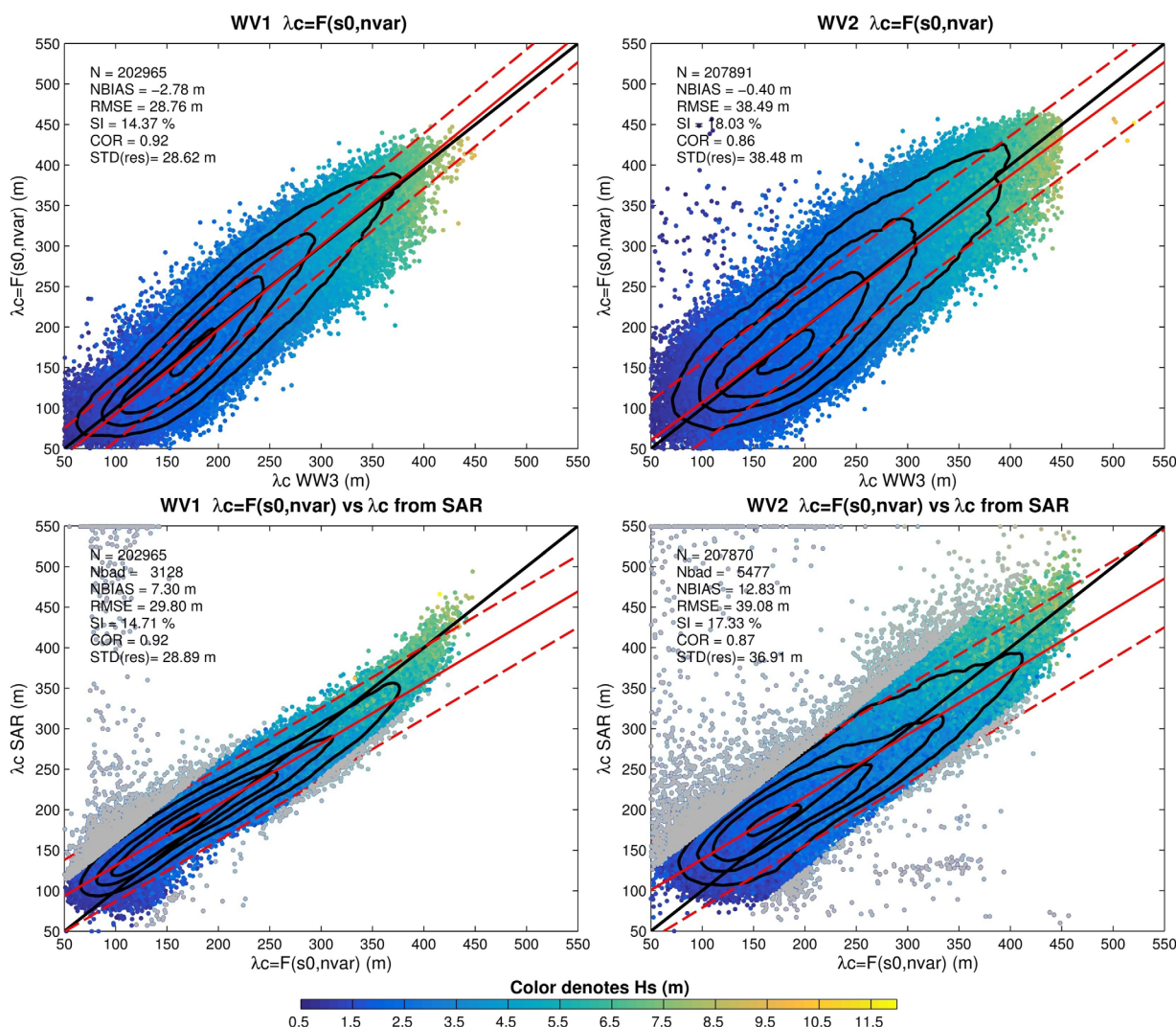


**Figure 4.** Comparison of WW3  $\lambda_c$  and an empirically derived function based on  $\sigma_0$  and  $nv$  for (top left) WV1 and (top right) WV2. Comparison of  $\lambda_c$  from the empirical model and measured by SAR for (bottom left) WV1 and (bottom right) WV2. The color denotes  $H_s$  in m from WW3. (bottom) The grey points are two standard deviations of the  $\lambda_c$  residuals between SAR and the empirical estimates about the one-to-one line.

3. Last we ensure the image is of good quality by comparing the calculated azimuth cutoff from the fitting the Gaussian function to an empirically derived GMF that is described in the following paragraph, 1–2% of original data set.

We created an empirical algorithm using the same training method described above to estimate the azimuth cutoff. We used two input parameters:  $\sigma_0$  and  $nv$  with two neurons in the hidden layer. We trained the data set using the azimuth cutoff computed from WW3 2-D wave spectra and include the geometrical effects and high-frequency contributions to make the WW3 azimuth cutoff comparable to S1A [Stopa *et al.*, 2015b]. Scatter plots of both WV1 and WV2 are given in Figure 4. There is a significant degradation in the performance of WV2 apparent by the larger dispersion. The bottom plots compare the SAR measurements and the empirical functions. Our purpose here is not to predict the most accurate azimuth cutoff nor to discuss the quality of this estimate in the ESA L2 product. We simply use the derived empirical functions to remove extreme cases where the difference between data and model is larger than 2 standard deviations of the residuals ( $\lambda_{c,Empirical} - \lambda_{c,WW3}$ ) for WV1 and WV2 is 30 and 37 m. The grey points in the bottom plots of Figure 4 represent the anomalous points removed.

### 3.3. CWAVE\_S1A Model

We follow the approach of *Schulz-Stellenflehth et al.* [2007] and decompose the SAR image spectrum in orthogonal harmonic components based on Gegenbauer polynomials and use  $\sigma_0$ , and  $nv$ . The full description of the decomposition is given in Appendix B. The 20 orthonormal parameters are computed from a normalized SAR wavenumber image spectra and capture the shape of the image spectra which contains information about the  $H_s$  as previously noted by [*Hasselmann and Hasselmann*, 1991]. We optimize the solution by varying the number of neurons and then computed standard error metrics such as the bias (BIAS), root mean square error (RMSE), correlation coefficients (R), the scatter index (SI), and the standard deviation of the residuals:

$$BIAS = \bar{x}_m - \bar{x}_t \tag{6}$$

$$RMSE = \sqrt{\frac{1}{n} \sum_{i=1}^n (x_{mi} - x_{ti})^2} \tag{7}$$

$$R = \frac{\sum_{i=1}^n (x_{mi} - \bar{x}_m)(x_{ti} - \bar{x}_t)}{\sqrt{\frac{1}{n} \sum_{i=1}^n (x_{mi} - \bar{x}_m)^2} \sqrt{\frac{1}{n} \sum_{i=1}^n (x_{ti} - \bar{x}_t)^2}} \tag{8}$$

$$SI = \left[ \sqrt{\frac{1}{n} \sum_{i=1}^n [(x_{mi} - \bar{x}_m) - (x_{ti} - \bar{x}_t)]^2} / \bar{x}_t \right] \times 100 \tag{9}$$

$$STD_{res} = \sqrt{\frac{1}{n} \sum_{i=1}^n ((x_{mi} - x_{ti}) - (\bar{x}_m - \bar{x}_t))^2} \tag{10}$$

where  $x_m$  and  $x_t$  are the developed model and independent testing data set that was not used in the training of the GMF. We varied the number of hidden neurons from 2 to 22 and found the RMSE were generally the same however we achieved the lowest SI of 18.29% with 10 nodes. Therefore we use  $N_n = 10$  for the development of our final neural networks. Since the radar response is dependent on incidence angle, separate functions are created for WV1 and WV2.

The final GMFs are created using approximately 3.5% of the WW3 colocations using the sampling approach described in section 3.1. Several GMFs are created and the best GMF is determined by minimizing the error metrics between the WW3 and satellite matchups that are not used in the development of the functions (the remaining 96.5%). The  $\sigma_0$  does not include a correction for the additive noise contribution from the antenna (equation (3)), which can be large for low wind speeds. When we include noise, there were only negligible differences in the performance of the GMFs. Therefore noise was not included in  $\sigma_0$  and in the final GMFs. It should be noted that, we observed a reduction of the GMF's scatter at low wave heights when the antenna noise is included in  $\sigma_0$  (not shown). The top plots of Figure 5 shows the entire data set including the training and validation samples used to create the GMFs. There is nearly a zero bias, high correlation of 0.92, scatter index of 18%, and RMSE of 0.5 m for WV1 and WV2. There is a small but discernible decrease in the performance of WV2. The least squares regression line agrees nicely with the one-to-one fit. We also analyzed the outliers defined when the residual is larger than 3 standard deviations ( $H_{sCWAVE} - H_{sWW3} > 3STD(H_{sCWAVE} - H_{sWW3})$ ). We found no spatial relationships and the points were uniformly dispersed across the globe (not shown). These results are similar with prior works of *Schulz-Stellenflehth et al.* [2007] and *Li et al.* [2011].

### 3.4. $F_{nm}$ Model

In addition to the CWAVE approach, we propose another method which relies on a reduced number of inputs that have more physical meaning. If we only consider  $\sigma_0$  and  $nv$  as already tested by *Schulz-Stellenflehth et al.* [2007], we find values of the same order of magnitude for correlation (0.87) and RMSE (0.66 m) (see Table 1). However, despite the fact, that the  $\sigma_0$ , which is the intensity of the backscattered signal, is strongly related to the ocean surface wind speed and that the  $nv$  reflects the intensity modulation due to the waves in the SAR image, these two parameters do not fully capture the nonlinearity of the imaging mechanism and the ocean wave response. To this aim, we add the azimuth cutoff since the parameter is a key indicator of the nonlinearities involved in the imaging mechanism and reflects the potential distortion

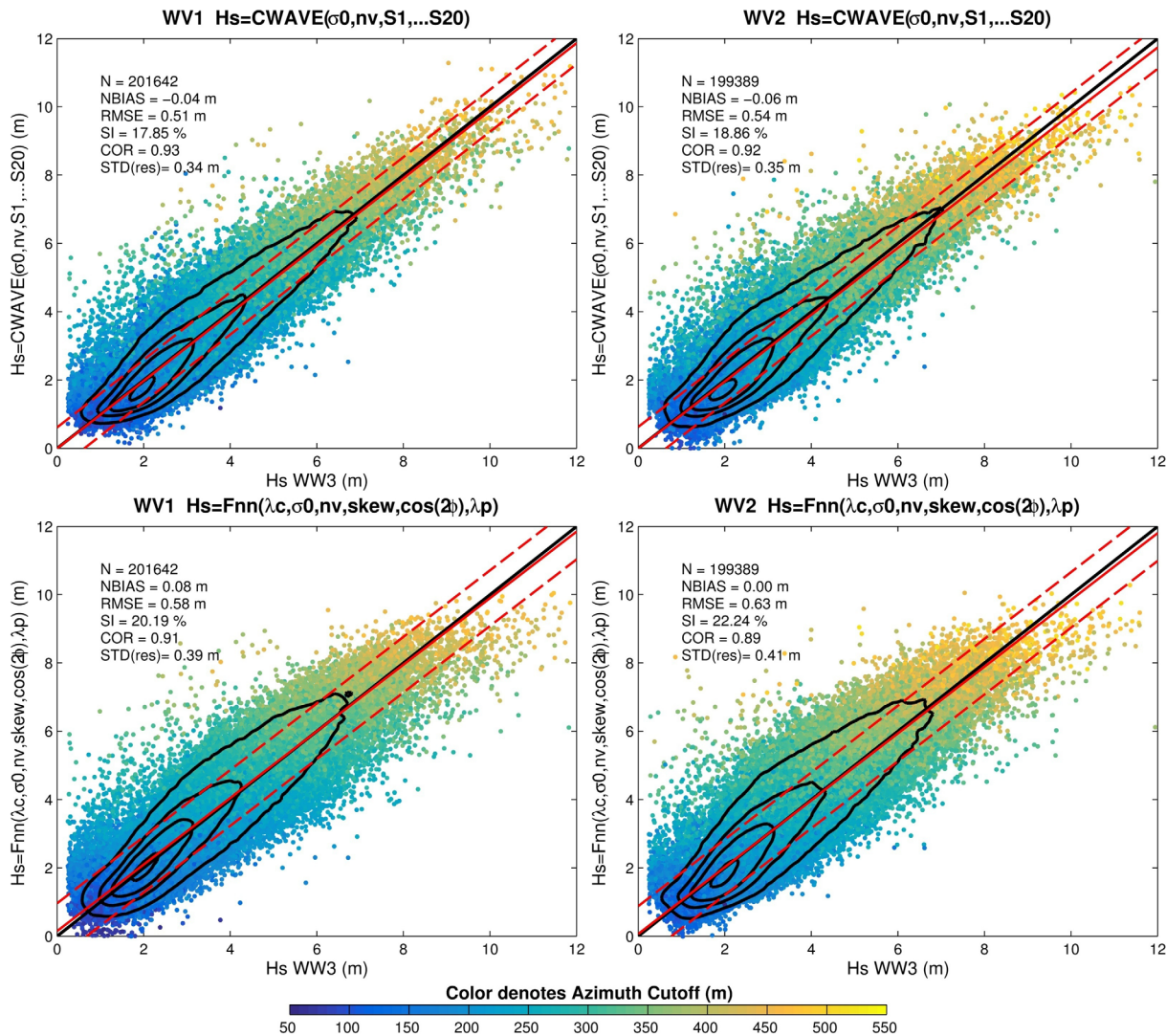


**Figure 5.**  $H_s$  comparison of WW3 and developed empirical functions excluding points collocated with buoys and altimeters: (top row) CWAVE\_S1A and (bottom row)  $F_{nn}$  for (left column) WV1 and (right column) WV2. The color represents the azimuth cutoff estimated from SAR, the contours represent 95, 75, 50, and 10% of data, solid red line represents a least square linear regression and the dashed lines represent 90% of the data.

**Table 1.**  $H_s$  WV1 Error Metrics for Development of Different Neural Networks Varying the Input Parameters Using WW3 Independent Colocations Not Used in Training of the Neural Network<sup>a</sup>

Model	$N_n$	BIAS (m)	RMSE (m)	SI (%)	R	$STD_{res}$ (m)
F( $\sigma_0, nv$ )	2	0.08	0.66	23.84	0.87	0.44
F( $\sigma_0, nv, skew$ )	3	0.03	0.64	22.52	0.88	0.43
F( $\sigma_0, nv, kurt$ )	3	0.03	0.64	22.62	0.88	0.43
F( $\sigma_0, nv, skew, kurt$ )	4	0.02	0.63	22.72	0.88	0.43
F( $\lambda_c, \sigma_0, nv$ )	3	0.03	0.62	22.49	0.88	0.43
F( $\lambda_c, \sigma_0, nv, skew$ )	4	0.01	0.61	22.30	0.89	0.42
F( $\lambda_c, \sigma_0, nv, skew, kurt$ )	5	0.00	0.61	22.36	0.89	0.42
F( $\lambda_c, \sigma_0, nv, skew, \lambda_p$ )	5	0.00	0.58	21.33	0.90	0.40
F( $\lambda_c, \sigma_0, nv, skew, \cos(2\phi)$ )	5	0.01	0.59	21.48	0.90	0.40
F( $\lambda_c, \sigma_0, nv, skew, kurt, \cos(2\phi)$ )	6	0.01	0.59	21.51	0.90	0.40
F( $\lambda_c, \sigma_0, nv, skew, \cos(2\phi), \lambda_p$ )	6	0.00	0.58	21.19	0.90	0.40
F( $\lambda_c, \sigma_0, nv, kurt, \cos(2\phi), \lambda_p$ )	6	0.00	0.58	21.25	0.90	0.40
F( $\lambda_c, \sigma_0, nv, skew, kurt, \cos(2\phi), \lambda_p$ )	7	0.00	0.61	21.21	0.90	0.40

<sup>a</sup>The errors metrics are the average of 25 different functions.

of the ocean waves spectrum. Previous studies show  $\lambda_c$  is related to  $H_s$  [Vachon et al., 1994; Kerbaol et al., 1998; Stopa et al., 2015b]. In addition, studies from Bruck and Lehner [2015]; Grieco et al. [2016]; Shao et al. [2016] rely on the strong relationship between  $\lambda_c$  and  $H_s$  to attempt a direct retrieval of  $H_s$  from the cutoff parameter. Both Grieco et al. [2016] and Shao et al. [2016] have a large range of incidence angles to consider and were strongly limited by the number of samples available to create robust estimators of wave heights in broad range of sea states. For a given cutoff, the distortion of observed ocean waves is not same with respect to the propagation direction of the wave system and peak wavelength. Therefore we include the peak direction ( $\phi$ —defined relative the satellite’s range direction) and peak wavelength ( $\lambda_p$ ) of the 2-D image spectrum coupled with the azimuth cutoff in our analysis. The peak wavelength and direction are computed from the absolute value of the cross spectrum from the SAR imagette and correspond to the maximum energy. Finally the important higher-order features are considered by skewness and kurtosis of the radar cross section

$$skew = \frac{1}{n} \sum_{i=1}^n (\sigma_{0i} - \overline{\sigma_0})^3 / s^3 \tag{11}$$

$$kurt = \frac{1}{n} \sum_{i=1}^n (\sigma_{0i} - \overline{\sigma_0})^4 / s^4 \tag{12}$$

where  $s$  is the standard deviation of  $\sigma_0$ .

Table 1 shows the error metrics from various developed neural networks based on different sets of input parameters. Using either skewness or kurtosis improved the predictability, however the inclusion of both parameters simultaneously is not necessary to improve the performance suggesting the information is redundant. When the azimuth cutoff is used as input, there is a significant improvement compared to the other functions that use three input parameters owing the strength of using  $\lambda_p$  as a sea state predictor. The use of either the skewness or kurtosis with  $\lambda_c$ ,  $\sigma_0$ , and  $nv$  improved the performance of the function. Finally the introduction of the angle and wavelength of the dominant wave energy significantly improved the performances by reducing the SI. We use  $\cos(2\phi)$  since Kerbaol et al. [1998] shows its important influence on  $\lambda_c$ . We find that using  $\lambda_c$ ,  $\sigma_0$ ,  $nv$ , skewness,  $\cos(2\phi)$ , and  $\lambda_p$  has the best performance with the lowest scatter index of 21.19% and RMSE of 0.58 m. Finally, we varied the number of hidden neurons and find that  $N_n = 6$  gave the best results. The coefficients of the developed functions for both WV1 and WV2 are given in the supporting information.

The results from the final functions are given in the bottom plots of Figure 5 containing the training, validation data sets, but excluding the points used for independent validation. Similar to the results obtained with CWAVE, this approach gives better results for WV1 than for WV2. We did not find any spatial biases when we analyzed the outliers of the residuals ( $H_{sFnn} - H_{sWW3} > 3STD(H_{sFnn} - H_{sWW3})$ ) (not shown). Compared to CWAVE the error metrics are slightly worse with correlation coefficients of 0.9, scatter index of 21%, and RMSE of 0.6 m. However, this algorithm only uses six input parameters instead of 22 for CWAVE. It should be mentioned that the training data sets used to create CWAVE and  $F_{nn}$  span the same sea states and thus we expect the sampling to have little impact on the resulting GMFs.

#### 4. Validation and Applications

Now with the developed functions we first compare the results to independent observations from altimeters and buoys. Second we analyze the GMFs performances through their ability to capture climate-scale statistics and represent wave heights larger than 8 m for both tropical and extratropical cyclones.

##### 4.1. Comparison With Independent Observations

Figure 6 shows the  $H_s$  comparison for the colocated altimeter data set. The results are similar to the WW3 comparison. For both approaches, WV1 performs better than WV2 and CWAVE\_S1A performs better than  $F_{nn}$ . The lower performances for WV2 are due to its weaker tilt modulation as well as lower signal to noise ratio which results in larger values of noise in  $\sigma_0$  and  $\lambda_c$ . Both techniques attain correlation coefficients larger than 0.90. The CWAVE\_S1A method provides very reliable wave heights with a RMSE of 0.5 m and SI less than 18% with nearly a zero bias. On the other hand,  $F_{nn}$  achieves a RMSE of 0.64 m and SIs less than 22.5%.

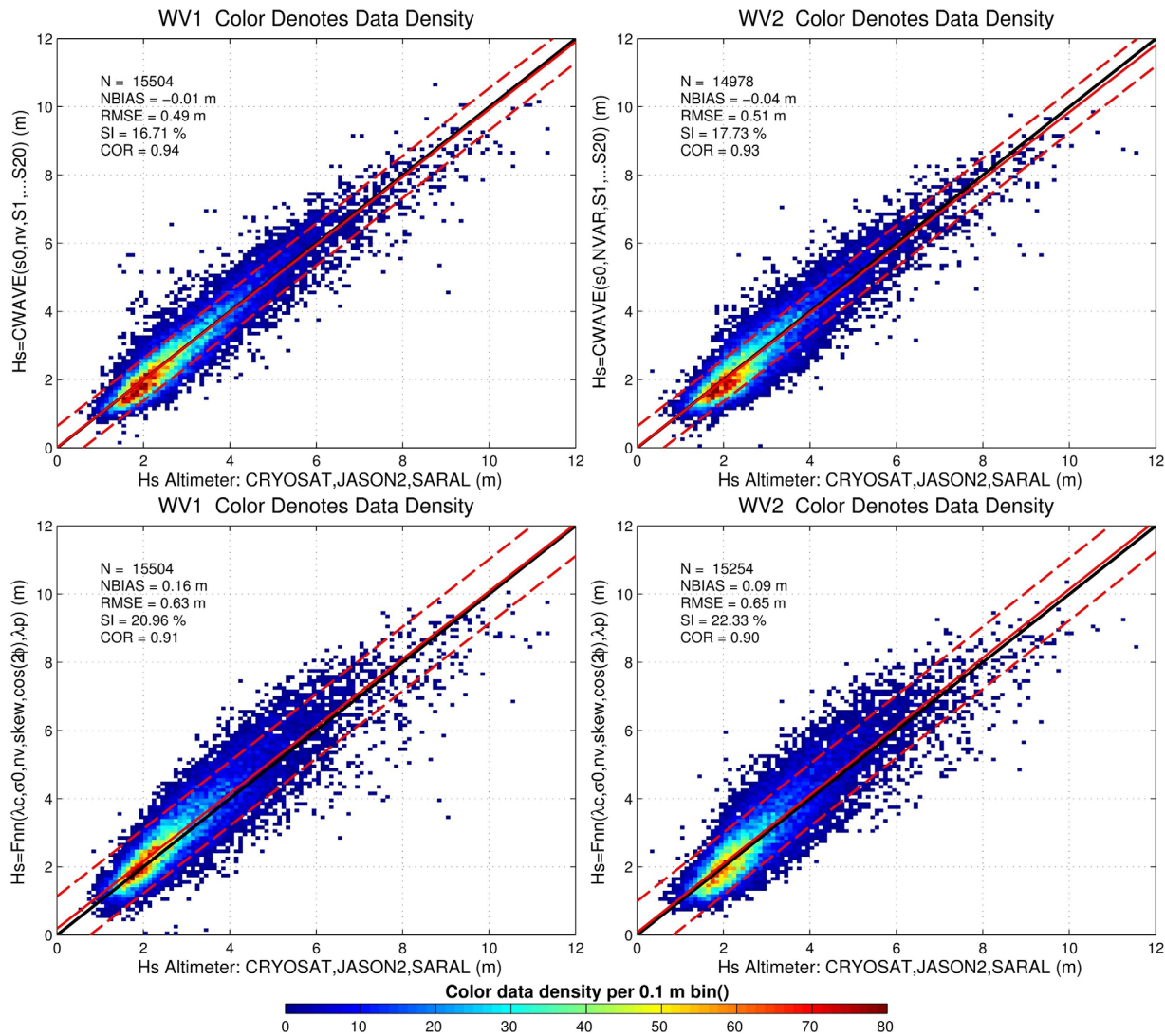


**Figure 6.**  $H_s$  comparison of the developed empirical functions: (top row) CWAVE\_S1A and (bottom row)  $F_{nn}$  for (left column) WW1 and (right column) WW2 with altimeter observations. The color represents the data density in 0.1 m bins, solid red line represents a least square linear regression, and the dashed lines represent 90% of the data.

There is a positive bias of 16 and 10 cm from WW1 and WW2 for  $F_{nn}$ . The dispersion of the errors is larger using  $F_{nn}$  (1.1 m) compared to CWAVE (0.85 m) shown by the dashed lines which contain approximately 90% of the data.

The same data are analyzed as a function of sea state and the residuals are computed for a given altimeter  $H_s$  shown in Figure 7. CWAVE performs well with nearly a zero bias from 1 to 8 m for both WW1 and WW2. When  $H_s$  is greater than 8 m a negative bias begins along with an increase in the precision as shown by the error bars representing one standard deviation of the residuals. Notice that for the most common sea state of 2 m, CWAVE works very well with high precision with errors of  $\pm 0.25$  m. The 10 cm positive bias of  $F_{nn}$  WW1 is now easily seen and for the range 1–6 m. In  $F_{nn}$  the positive bias of WW2 is reduced. When  $H_s > 6$  m a negative bias begins and gradually increases as the sea state becomes larger with a bias of 0.8 m for  $H_s > 9$  m. Also notice that all models have a small positive bias for  $4 \leq H_s \leq 6$  m and this feature is more pronounced in  $F_{nn}$ .

We provide error metrics for different environmental conditions in Table 2. For small sea states ( $H_s < 1$  m) we see that the GMFs have reduced performances with correlation coefficients less than 0.3 and reduced precision shown by the larger SIs. We expect that if the antenna noise is included in the  $\sigma_0$  then the scatter will reduce. When the sea state is large ( $H_s > 8$  m), all GMFs underestimate the wave heights by at least 0.75 m with RMSE of 1.3 m. Despite these larger errors both techniques provide reliable  $H_s$  estimations

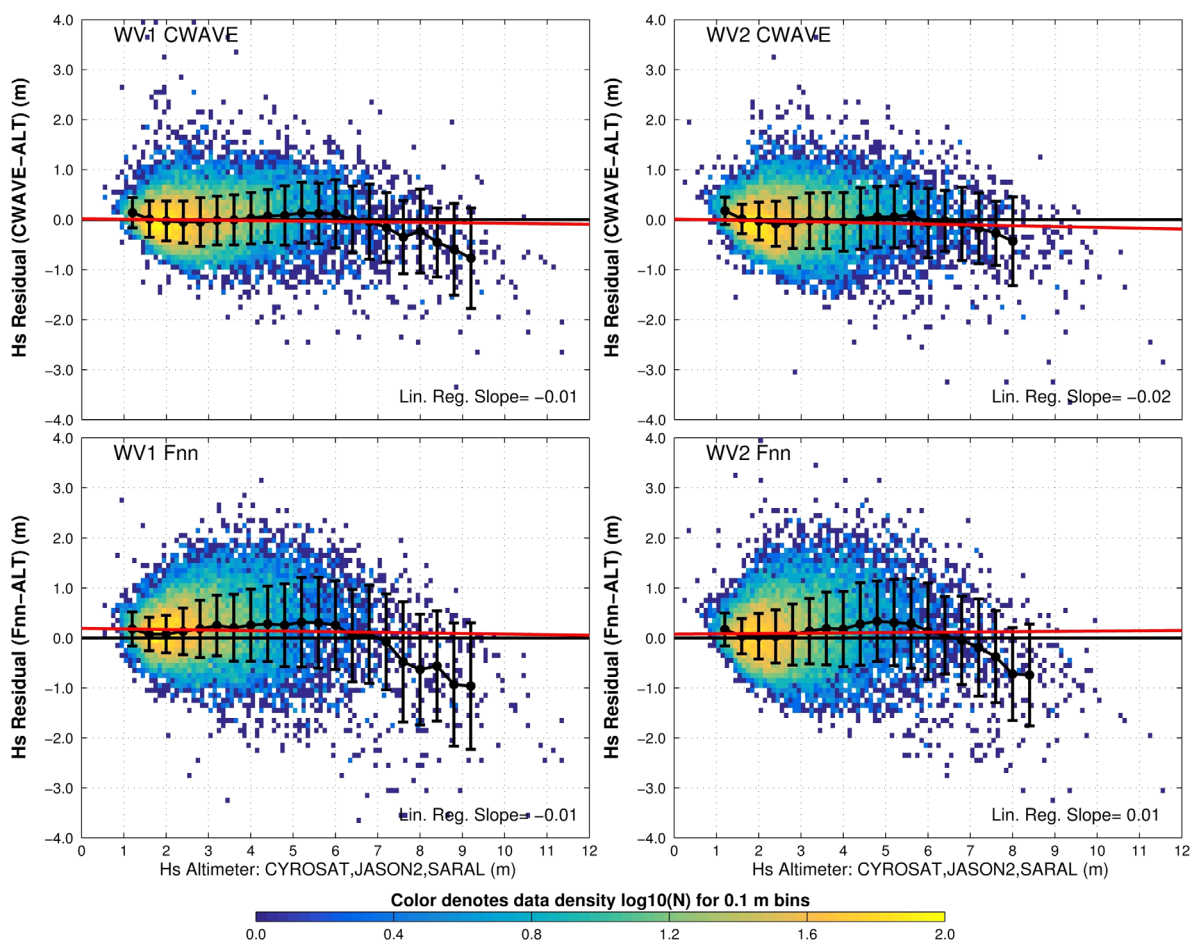


**Figure 7.**  $H_s$  residuals as a function of sea state from altimeters and developed empirical functions: (top row) CWAVE\_S1A and (bottom row)  $F_{nn}$  for (left column) WW1 and (right column) WW2. The color represents the data density on a logarithmic scale, the line represents the bias for each bin, and the error bars represent the standard deviation of residuals.

shown by the SIs that are less than 13%. In shallow water environments (when the depth,  $Z < 100$  m), all GMFs perform well suggesting the methods works well near coastlines where engineering applications are more common. Actually for CWAVE there is improved performance compared to the overall statistics while for  $F_{nn}$  the performance worsens. As a last comparison the distance of the colocations is limited to 50 km and the overall statistics are nearly the same which is typical of wave conditions which tend to evolve on slow time scales.

Finally, we compare the developed GMFs to in situ buoy  $H_s$  observations in Figure 8. The error metrics have similar correlation coefficients but have larger RMSEs of 0.6–0.7 m and SIs of 20–24% and are comparable

**Table 2.**  $H_s$  Error Metrics Using Altimeter Data Various Conditions for CWAVE\_S1A and  $F_{nn}$  (in Parentheses) for WW1 and WW2

	N	BIAS (m)	RMSE (m)	SI (%)	R	$STD_{res}$ (m)
<b>WW1 CWAVE (Fnn)</b>						
All	15,504	-0.01 (+0.16)	0.49 (0.63)	16.71 (20.96)	0.94 (0.91)	0.33 (0.43)
$H_s < 1$ m	66	+0.16 (+0.28)	0.26 (0.41)	22.72 (34.37)	0.16 (0.16)	0.15 (0.25)
$H_s > 8$ m	118	-0.76 (-0.96)	1.23 (1.53)	10.69 (13.27)	0.50 (0.40)	0.83 (1.04)
$Z < 100$ m	37	-0.07 (+0.13)	0.37 (0.54)	16.62 (23.43)	0.94 (0.89)	0.24 (0.32)
$DX < 50$ km	7801	-0.01 (+0.16)	0.47 (0.63)	16.07 (20.56)	0.95 (0.91)	0.31 (0.42)
<b>WW2 CWAVE (Fnn)</b>						
All	14978	-0.04 (+0.09)	0.51 (0.65)	17.73 (22.35)	0.93 (0.90)	0.33 (0.42)
$H_s < 1$ m	65	+0.30 (+0.30)	0.46 (0.48)	40.99 (43.65)	0.24 (0.30)	0.29 (0.32)
$H_s > 8$ m	80	-0.79 (-0.94)	1.16 (1.34)	9.64 (10.71)	0.44 (0.42)	0.78 (0.82)
$Z < 100$ m	20	-0.04 (+0.12)	0.40 (0.69)	17.00 (29.05)	0.96 (0.88)	0.23 (0.47)
$DX < 50$ km	7501	-0.04 (+0.09)	0.50 (0.64)	17.23 (21.95)	0.93 (0.90)	0.32 (0.42)

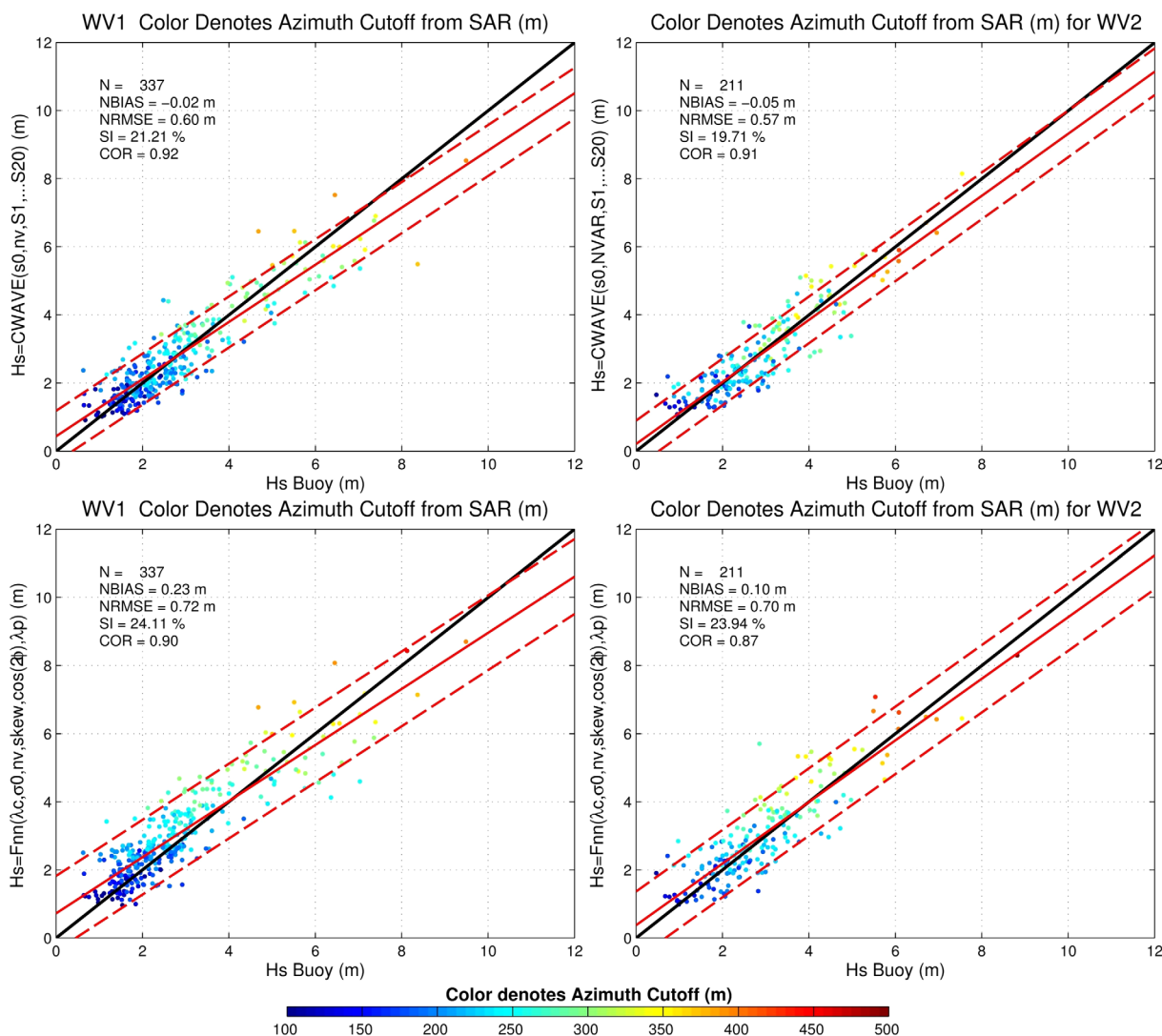


**Figure 8.**  $H_s$  comparison of the developed empirical functions: (top row) CWAVE\_S1A and (bottom row)  $F_{nn}$  for (left column) WV1 and (right column) WV2 with buoy observations. The color represents the azimuth cutoff estimated from SAR, solid red line represents a least square linear regression, and the dashed lines represent 90% of the data.

to Li *et al.* [2011]. In all cases, the upper wave heights are underestimated causing the negative slope of the linear regression line. In general both algorithms provide reliable  $H_s$  retrievals.

#### 4.2. Applications: Climate and Case Studies

In this section, we demonstrate the added benefit of using our proposed GMFs to describe wave statistics on long-time scales and retrieve wave information in high sea states. First, we compare monthly averages obtained with our developed GMFs to altimeter data. In Figure 9 we display the monthly average of July and December 2015 to represent the seasonal variations in the wave field. The statistics are computed using  $2.5^\circ$  bins for both satellite technologies. The altimeters have approximately 650 points per bin while S1A has approximately 30 per bin using both WV1 and WV2. To equalize the sampling and allow a fair comparison between the two, we take a random permutation of 30 samples from the altimeter data set. The procedure is repeated 25 times and these results are averaged and used to represent the altimeter data. In December the wave heights are largest in the Northern Hemisphere and the GMFs match the  $H_s$  magnitudes. Qualitatively the GMFs match the altimeter observations well. In the Southern Indian Ocean CWAVE and  $F_{nn}$  have larger wave heights than the altimeter data and this is more pronounced in  $F_{nn}$ . In July, the pattern reverses and larger wave heights are observed in the Southern Hemisphere. These results have similar magnitudes and patterns as presented for December–January–February and June–July–August using a

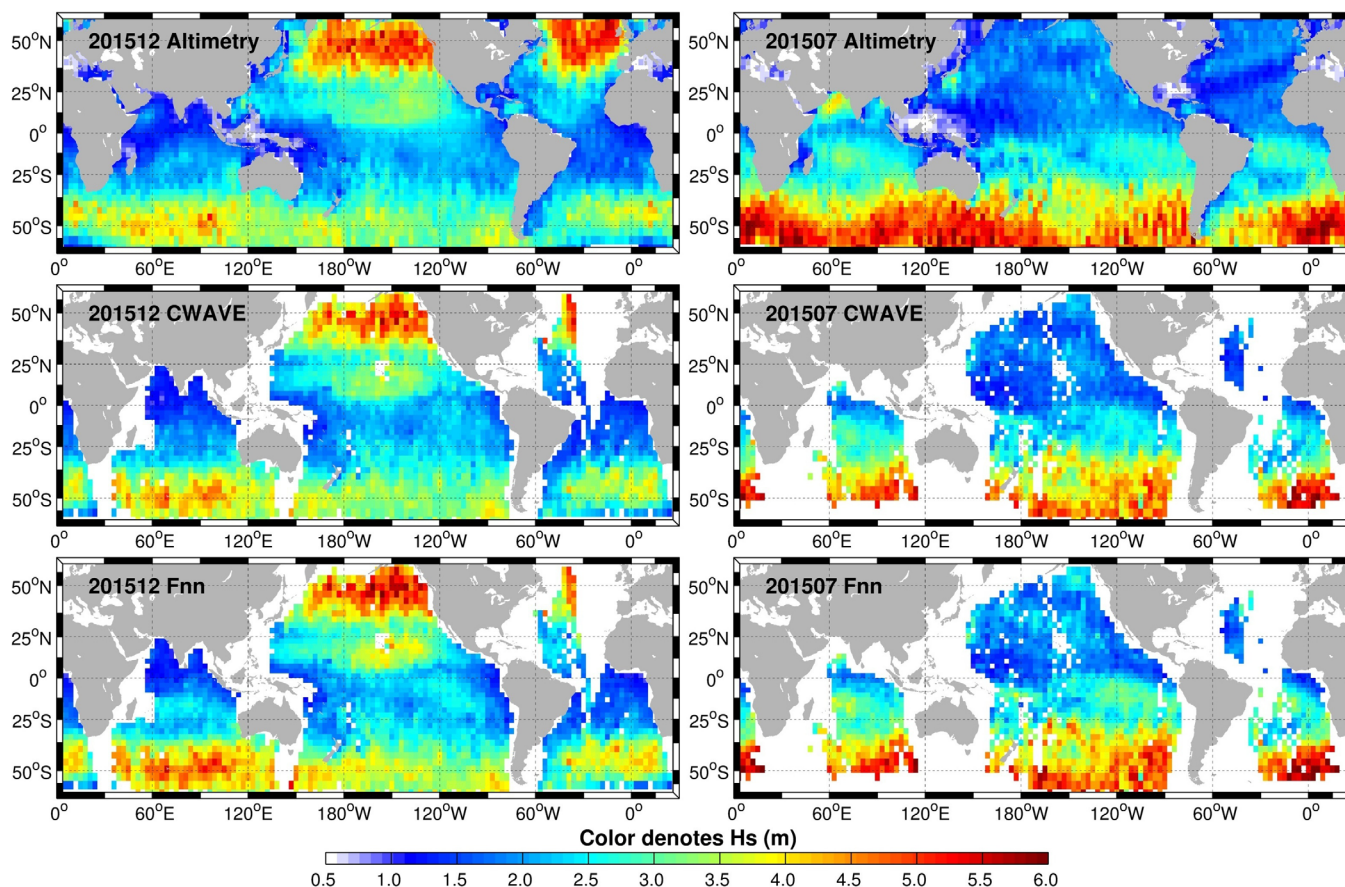


**Figure 9.**  $H_s$  averages for (left) December and (right) July 2015 from (top row) altimeters and developed empirical functions: (middle row) CWAVE and (bottom row)  $F_{nn}$  combining WV1 and WV2 in  $2.5^\circ$  bins.

wave hindcast of CFSR [Stopa *et al.*, 2013]. Both CWAVE and  $F_{nn}$  qualitatively match the wave heights despite the missing data. Therefore we expect the developed algorithms to effectively aide in the description of statistics for long-time series, by complementing existing SAR and altimeter archives.

Next we provide two case studies in September 2015 to demonstrate the added benefit of using our developed GMFs to retrieve wave information in poorly sampled high sea states. These cases were not used in the training of the GMFs. The 2015 Pacific tropical cyclone season was the second most active Pacific season on record. Three of these major Hurricanes: Kilo, Ignacio, and Jimena were active from 20 August through 10 September. S1A crosses Hurricane Jimena in the North Tropical Pacific on the first of September shown in Figure 10. The background color represents the  $H_s$  computed from WW3 using ECMWF wind forcing. Kilo near  $180^\circ\text{W}$  and Ignacio near  $154^\circ\text{W}$  can be seen in the western portion of the basin. The bottom two plots compare the derived  $H_s$  from both algorithms. We can see that both techniques reproduce the increase of the sea state due to the tropical cyclone generated waves. However, for WV1 both SAR models underestimate the peak of the event by approximately 2 m. In WV2, the proposed algorithms are slightly overestimating the peak of the event by 1 m. Since WV1 and WV2 are, respectively, underestimating and overestimating the waves in their respective tracks it suggests the location of the storm is incorrect in the global model of ECMWF. We should also mention that our model setup using ECMWF winds underestimates the maximum wind speeds compared to satellite observations from scatterometers and L-band radiometers of Reul *et al.* [2016] (not shown). Furthermore, the spatial resolution of the global wave model at  $0.5^\circ$  is not able to properly describe the storm's important features because the storms have an approximate radius of maximum winds near 30–50 km. From our previous analysis in section 4.1, it is clear that the GMFs underestimate the largest  $H_s$ . Notice far from the storm, CWAVE and  $F_{nn}$  match the wave heights well and are typically within  $\pm 35$  cm of WW3. We were not able to find any satellite passes in the GlobWave altimeter database within close time and space constraints ( $< 3$  h) that could cross validate these results.

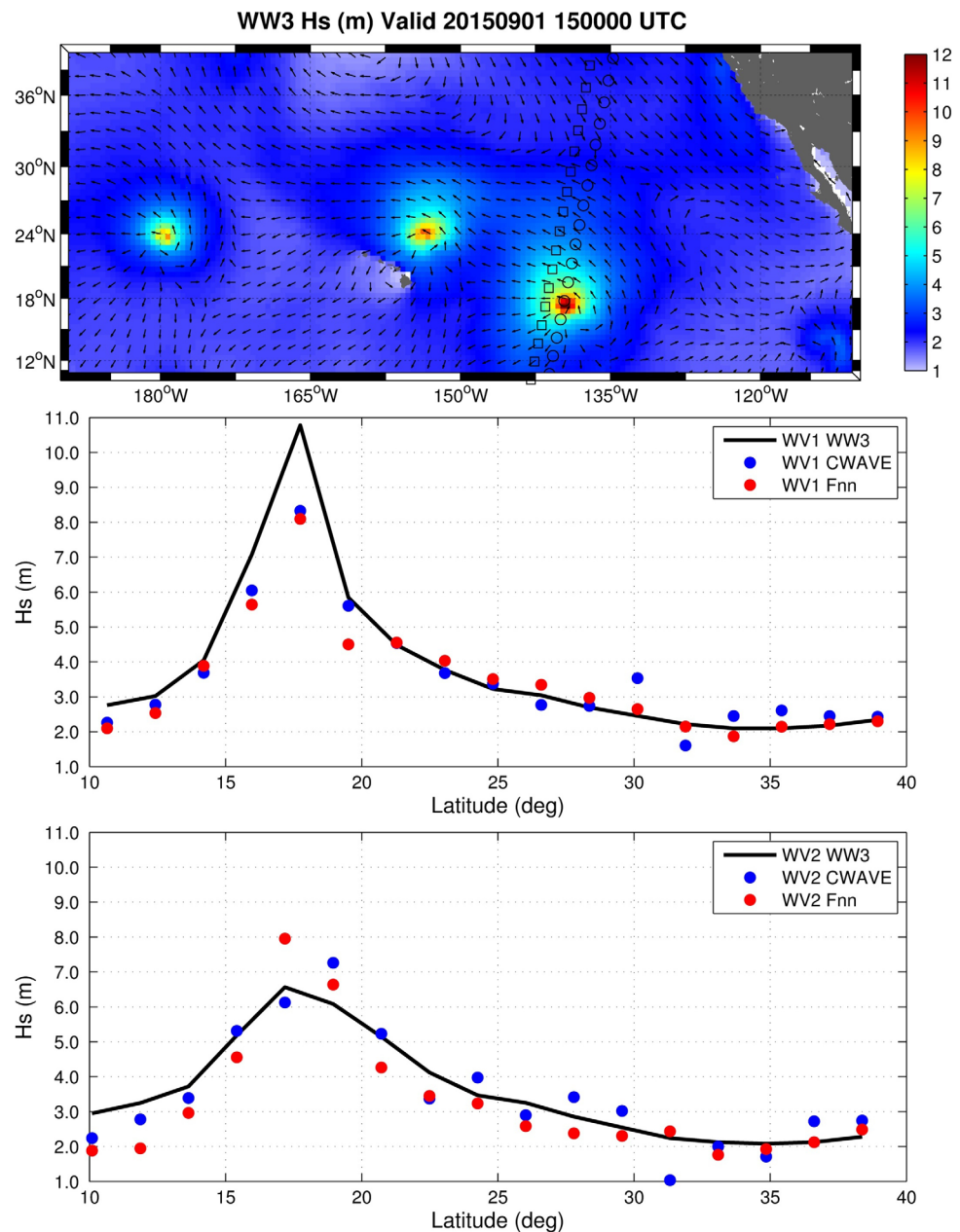


**Figure 10.** S1A and WW3  $H_s$  comparison for Hurricane Jimena on 1 September 2015. The colors represent  $H_s$  and arrows represent average wave directions from WW3 with (top) S1A satellite pass, (middle) WV1 transect, and (bottom) WV2 transect containing CWAVE,  $F_{nn}$ , and WW3.

The second event shows a rather typical extratropical storm in the Southern Ocean in the Indian Ocean sector in Figure 11. Compared to the previous example the wave field is much smoother and the region of wave heights above 10 m is much larger. In this case for both WV1 and WV2, CWAVE and  $F_{nn}$  match the magnitude of the event very well and are within 25 cm of the 9.5 m wave height. In this case the SARAL altimeter passed over the same area 1 h earlier at 11:00 UTC. Notice that the peak of the event is in agreement between the altimeter, SAR, and WW3 for WV1 noting the difference in timing between SARAL and S1A. The middle plots of Figure 1 correspond to the event maximum for WV1 seen in the second point of Figure 11 at 54°S. The azimuth cutoff is large (430 m) and does not allow any waves below this value to be properly resolved. So in this case, the quasi-linear approach to retrieve ocean swell spectra cannot provide any reliable wave estimates. This shows the added benefit of using these empirical methods to estimate

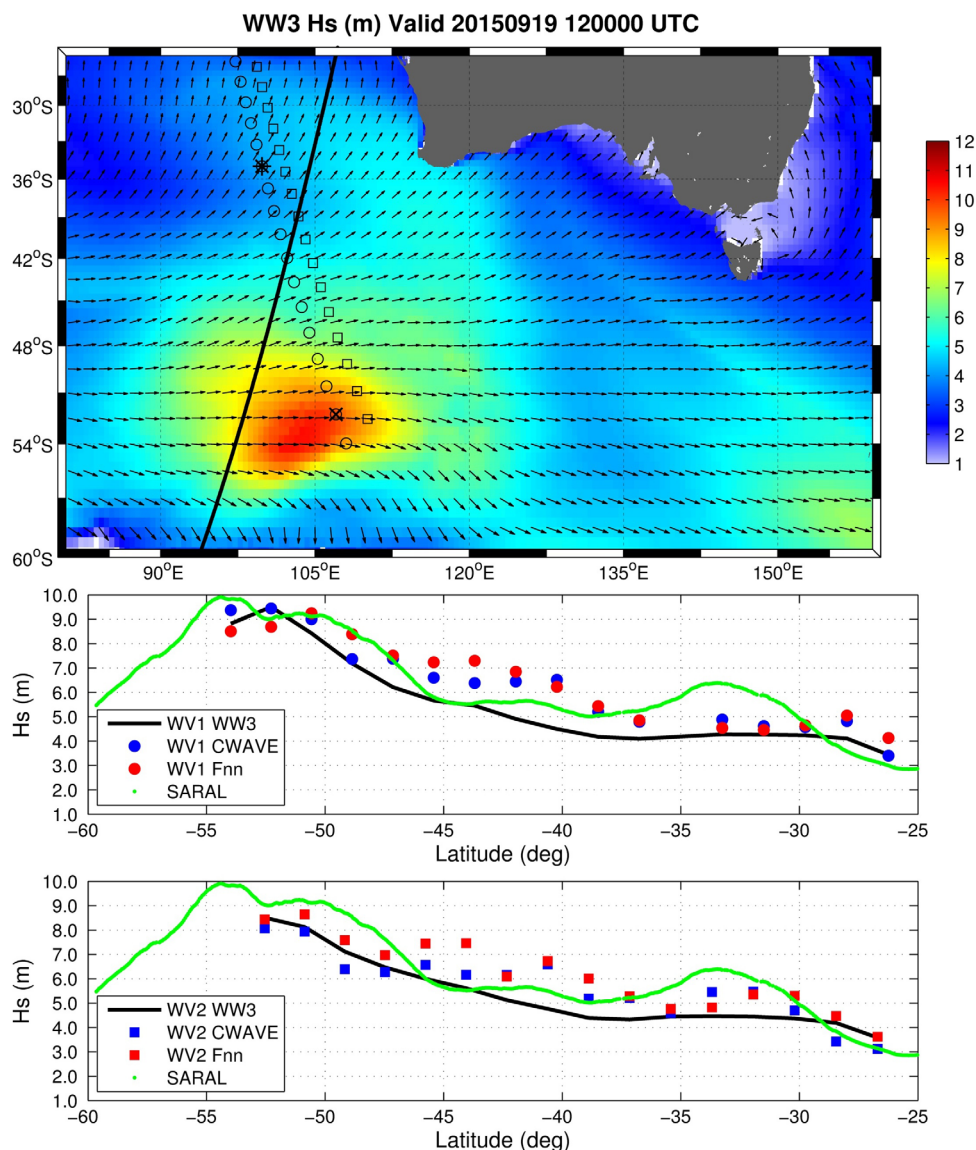


**Figure 11.** S1A and WW3  $H_s$  comparison for a storm in the Southern Indian Ocean 19 September 2015. The colors represent  $H_s$  and arrows represent average wave directions from (top) WW3 with S1A and SARAL satellite passes, (middle) WV1 transect, and (bottom) WV2 transect containing CWAVE,  $F_{nn}$ , and WW3. The black “x” and “\*” correspond to the middle and right plots of Figure 1, respectively.

wave properties in severe sea states. The ECMWF wind field and WW3 certainly do not capture the detailed features far from the storm and model outputs are relatively smooth compared to the satellites. For latitudes from 45 to 35°S both GMFs disagree with WW3 and estimate the wave heights 2 m larger than WW3. Otherwise the GMFs and WW3  $H_s$  are within  $\pm 1$  m. There is no noticeable bias between CWAVE and  $F_{nn}$ .

### 5. Discussion

Both empirical methods, CWAVE and  $F_{nn}$ , estimate reliable significant wave heights. The CWAVE approach effectively decomposes the shape of the image spectrum into different components that contain useful sea state information extending the works of Schulz-Stellenfleh et al. [2007] and Li et al. [2011] to S1A. Our error metrics are similar to these two works which were based on ERS2 and Envisat. The S1A sensor has a larger footprint and higher nominal spatial resolution; however, this does not seem to drastically improve the results. The lower wavelength used for CWAVE\_ERS2 and CWAVE\_ENV was 60 m. We lowered this value to

30 m since the S1A is able to resolve these wavelengths, but we did not see any improvement in the performance of the resulting GMFs.

CWAVE performs better than  $F_{nn}$  with improved error metrics but has nearly four times the amount of input parameters. In the future, it is beneficial to systematically assess the most important input parameters from CWAVE to reduce the number of inputs. This might provide new insights between the environmental conditions and the observation SAR image spectra. Ultimately this might improve our understanding of the SAR imaging process. This was already one of the motivations to create  $F_{nn}$  which relies on a reduced number of physical parameters. For this GMF, we use the azimuth cutoff,  $\sigma_0$ ,  $nv$ , skewness, peak wave length, and peak direction of the SAR image to estimate  $H_s$ . These input parameters seem to capture most of the essential sea state information to derive  $H_s$ .

While we only focused on  $H_s$  in the text, we developed similar empirical functions to estimate wave periods like Tm-10, Tm01, and Tm02. See the Appendix C for further information. The proposed methods cannot estimate wave periods as accurately as  $H_s$ . This might be due to the multivalued nature of average wave periods. Like Schulz-Stellenfleth *et al.* [2007], Tm02 performed worse than other estimates of the wave period and might be due to the stronger dependence on higher wave frequencies. Our wave period error metrics agree with those of both Schulz-Stellenfleth *et al.* [2007] and Li *et al.* [2011]. However the scatter plots presented in Li *et al.* [2011] seem to have reduced scatter compared to our results. In the future, we will pursue efforts in estimating wave periods and also other important wave parameters like wave energy, the wind sea component, and the Stokes drift. These are important parameters for engineering and scientific communities interested in renewable energy and air-sea dynamics.

ECWMF wind speeds, which are similar to ERA-Interim are expected to underestimate the large wave events [Stopa and Cheung, 2014]. In addition, the WW3 grid resolution of  $0.5^\circ$  might be too coarse to describe important space-time features associated with wave development important for extreme events. Therefore, we expect some of the underestimation when  $H_s > 8$ , is related to the using this model setup. In the future, it may become possible to better resolve the extreme waves with WW3 by directly forcing with more realistic winds such as composite satellite winds from radiometers as SMOS [Reul *et al.*, 2016] and AMSR-2 [Zabolotskikh *et al.*, 2016] or by using wind models that assimilate these products. We placed a lot of emphasis on adequately sampling the extreme wave events in the training of our GMFs. Our initial data set was composed of 260,000 colocations between WW3 and S1A. Despite this extensive number of colocations, we still had only few events with  $H_s > 12$  m; so it is expected that the GMFs may perform poorly with larger wave heights. On the contrary, the case studies shown in Figures 10 and 11 demonstrate that both algorithms can estimate wave heights larger than 9 m, which is encouraging.

In addition to training with WW3, we also developed GMFs using the altimeter data set with 16,000 data pairs collected over 6 months. The altimeter  $H_s$  probability distribution is similar to the top plots of Figure 3 and there is a 40% chance of having  $1.5 \leq H_s \leq 2.5$  and only a 0.6% change of having a wave height larger than 8 m. The altimeter-trained GMFs have a significant degradation in performance. Despite differences between WW3 and altimeter measurements, we believe that the undersampling explains the poor altimeter-trained GMF performance. The recent launch of Sentinel-3 A and JASON-3 (2016) and the forthcoming launches of Sentinel-3 B (2017), CFOSAT (2018) will certainly offer the possibility to rely on sufficient amount of altimeter data for future work.

Compared to Schulz-Stellenfleth *et al.* [2007] and Li *et al.* [2011], we use neural networks instead of a linear regression with cross terms. It seems that this reduces the number of coefficients needed and allows for a more compact solution. Otherwise the performance is nearly identical.

The proposed empirical models clearly extend the number of geophysical variables related to waves that are available from the ESA OCN L2 SAR product. The monthly averages seem to reasonably match the statistics of the altimeter data set and the continued operation of the Sentinel missions will allow for climate studies especially when merged with data from altimeter missions. The  $H_s$  can be retrieved for a larger range of sea state conditions than ESA's swell spectra. This includes situations with strong distortion created by the azimuth cutoff and would prevent any accurate ocean swell spectrum retrieval. There are certainly opportunities to use this new information in the ocean swell spectrum inversion scheme such as the retrieval of the wind sea component. Furthermore the independent estimation of wave parameters from SAR may improve the quasi-linear inversion scheme by more precisely estimating the non-linear (wind-sea)

component. We demonstrate through two examples the ability of the GMFs to estimate wave heights in tropical and extra tropical storms. Effectively this allows the SAR sensor to complement existing wave observations from buoys, altimeters, and ship observations. Finally, it should be noted that our GMFs can directly be applied to the identical S1B SAR.

## 6. Conclusions

We successfully estimated significant wave heights and wave periods using two different empirical approaches without external information. The first approach, CWAVE, effectively decomposes the shape of the image spectrum into orthogonal components that capture the important effects distorted by the SAR imaging. The second approach uses a reduced number of input parameters including the azimuth cutoff and is able to replicate the results with reasonable accuracy. Both methods can be applied globally and are expected to predict the sea state parameters when  $0.25 \leq H_s \leq 13$  m. When the wave heights were larger, we were not able to effectively address the performance of the GMFs, but as more data are routinely collected from S1A and now from the identical S1B we will be able to refine the proposed model performances in the near future. We use variables included in ESA's L2 product and the neural networks are computationally efficient allowing ease of computing the parameters.

We trained using model data generated from WW3 and independently compared to both altimeter and buoy measurements. This effectively demonstrated the ability of WW3 to resolve the sea state conditions with zero bias under the most probable average sea states we encountered. We achieved RMS less than 0.5 and 0.6 m for CWAVE and  $F_{nn}$ , respectively, and the functions are expected to perform equally well for deep and shallow waters.

Observations from space-borne remote sensing continually shape our understanding of the Earth's dynamics by providing important space-time information. The high resolution of SAR effectively resolves a large amount of geophysical information that can be used for a large range of applications. For instance, the now standard techniques of *Hasselmann et al.* [1996] and *Chapron et al.* [2001] to retrieve ocean wave spectra from image spectra have aided in the understanding of the wave dynamics. However comparing SAR observations to other sources of information using the standard wave parameter of  $H_s$  is still not possible. This motivated *Schulz-Stellenfleth et al.* [2007] among others to develop empirical functions to exploit useful wave information contained in the SAR images. In this study, we demonstrate that integral wave parameters can be retrieved from the S1A platform at the global scale. While our study was limited to the Sentinel-1 SAR our methodology can be applied to any of the other currently available SAR data from Radarsat-2 and Gaofen-3 (C-band), TerraSAR-X and Cosmo-SkyMed (X-band), and ALOS-2 (L-band) some of which have a dedicated acquisition mode for measurements of ocean wave spectra. With the newly available S1A and S1B measurements and the ability of the algorithms to provide reliable wave estimates in a large range of environmental conditions we make better use of the SAR measurements for practical applications.

## Appendix A: Training Using Neural Networks

A multilayer perceptron (MLP) neural network is a widely used technique to predict any outcome. When the technique is combined with backpropagation of errors, it provides a powerful solution to numerous applications [*Hagan et al.*, 2014]. We empirically determined that a three layer MLP consisting of an input layer, one hidden layer, and an output layer performs well. The number of neurons for each developed neural network in the hidden layer are determined empirically by reducing errors. We use a tan-sigmoid function transfer function

$$\text{tansig}(\mathbf{x}) = 2[1 + \exp(-2\mathbf{x})]^{-1} - 1 \quad (\text{A1})$$

between both the hidden and output layers where  $\mathbf{x}$  is the input vector. The tan-sigmoid function is chosen because the outputs become asymptotic at the input extremes, therefore in each layer can only saturate to 0 or 1 and will not overwhelm the following MLP stage. This attenuating property of the tan-sigmoid function allows representation of the nonlinear relationships [*Gourrion et al.*, 2002]. The input matrix,  $\mathbf{X}$ , is organized by having M number rows and N number of columns with size (M,N). The input vector is normalized

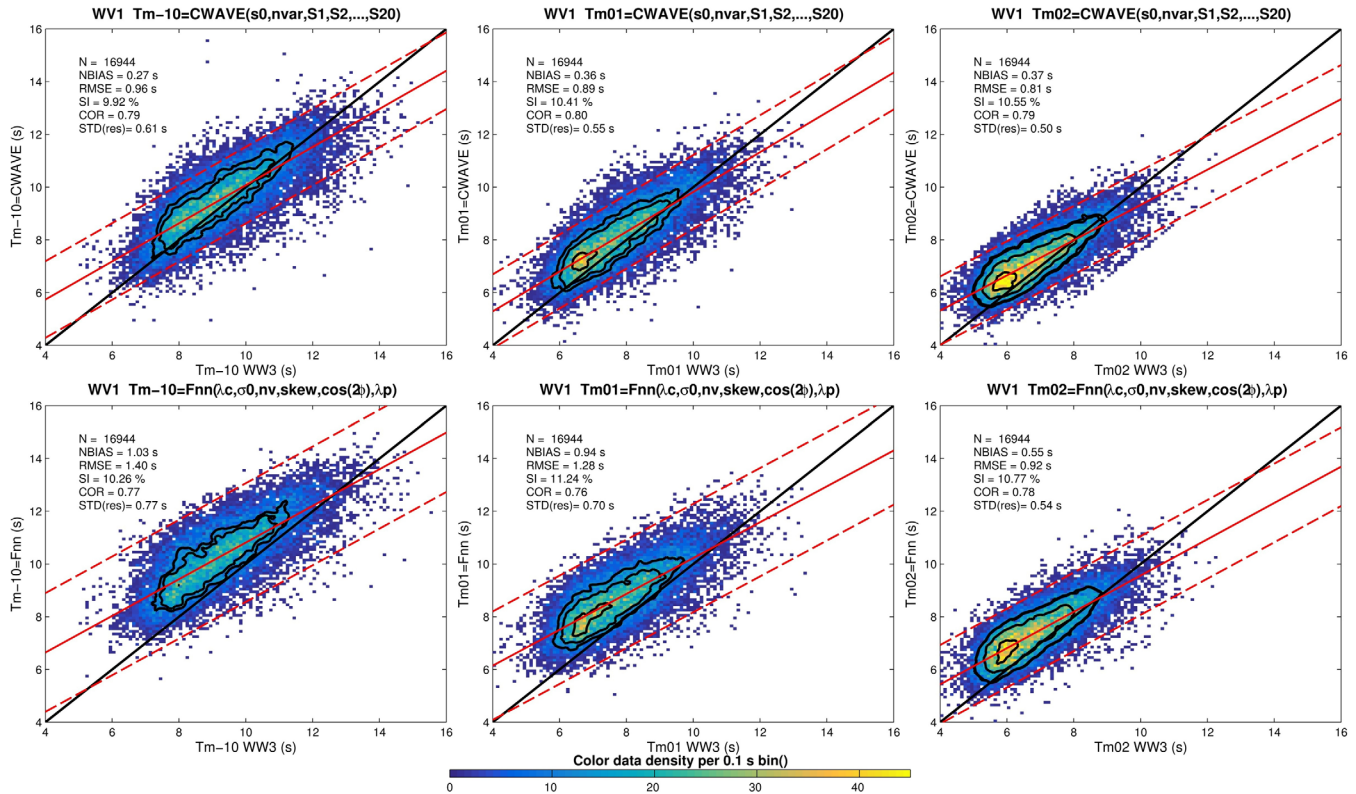


**Figure C1.** Average wave period comparison for September 2015 for WW1. (top) CWAVE and (bottom)  $F_{nn}$  for three different average wave periods. The color represents the data density in 0.1 s bins, solid red line represents a least square linear regression, and the dashed lines represent 90% of the data.

$$X_n = 2[(X - X_{\min}) / (X_{\max} - X_{\min})]^{-1} - 1 \quad (A2)$$

where  $\mathbf{O}$  is a vector of ones with size  $(1, N)$ . The normalized output  $Y_n$  is calculated

$$Y_n = L_w \text{tansig}(l_w X_n + B_1) + B_2 \quad (A3)$$

where  $l_w$  are the input weights of size  $(N_n, 1)$ ,  $L_w$  are the layer weights of size  $(1, N_n)$ ,  $B_1$  are the biases for the first hidden layer of size  $(N_n, 1)$  and  $B_2$  is the bias for the single output layer of size  $(1, 1)$ , and  $N_n$  is the number of hidden neurons that are determined by trial and error in order to minimize the overall error and precision of the fitted functions. Finally the output in the correct respective units is calculated

$$F_{nn} = [Y_{\min} + (Y_{\max} - Y_{\min})(Y_n + 1)/2]^T \quad (A4)$$

where  $Y_{\min}$  and  $Y_{\max}$  are the minimum and maximum of the training data set and  $^T$  denotes the matrix transpose.

### Appendix B: Orthogonal Functions Used in CWAVE

We construct the following orthogonal functions based on the S1A image spectrum  $\bar{P}$  normalized by the total energy as

$$\bar{P} = P / \sum (P * dk_x * dk_y) \quad (B1)$$

where  $dk_x$  and  $dk_y$  are the wavenumber spacing. We compute the scalar products,  $S$  from  $\bar{P}$  using the orthogonal functions  $\bar{h}_{ij}$

$$S_{ij} = \sum \bar{P}(k_x, k_y) \bar{h}_{ij}(k_x, k_y) dk_x dk_y \quad (B2)$$

where  $1 \leq i \leq n_\phi n_k$ . The orthogonal functions  $\bar{h}_{ij}$  are composed of Gegenbauer polynomials  $g_i(\alpha_k)$  and harmonic functions  $f_j(\alpha_\phi)$

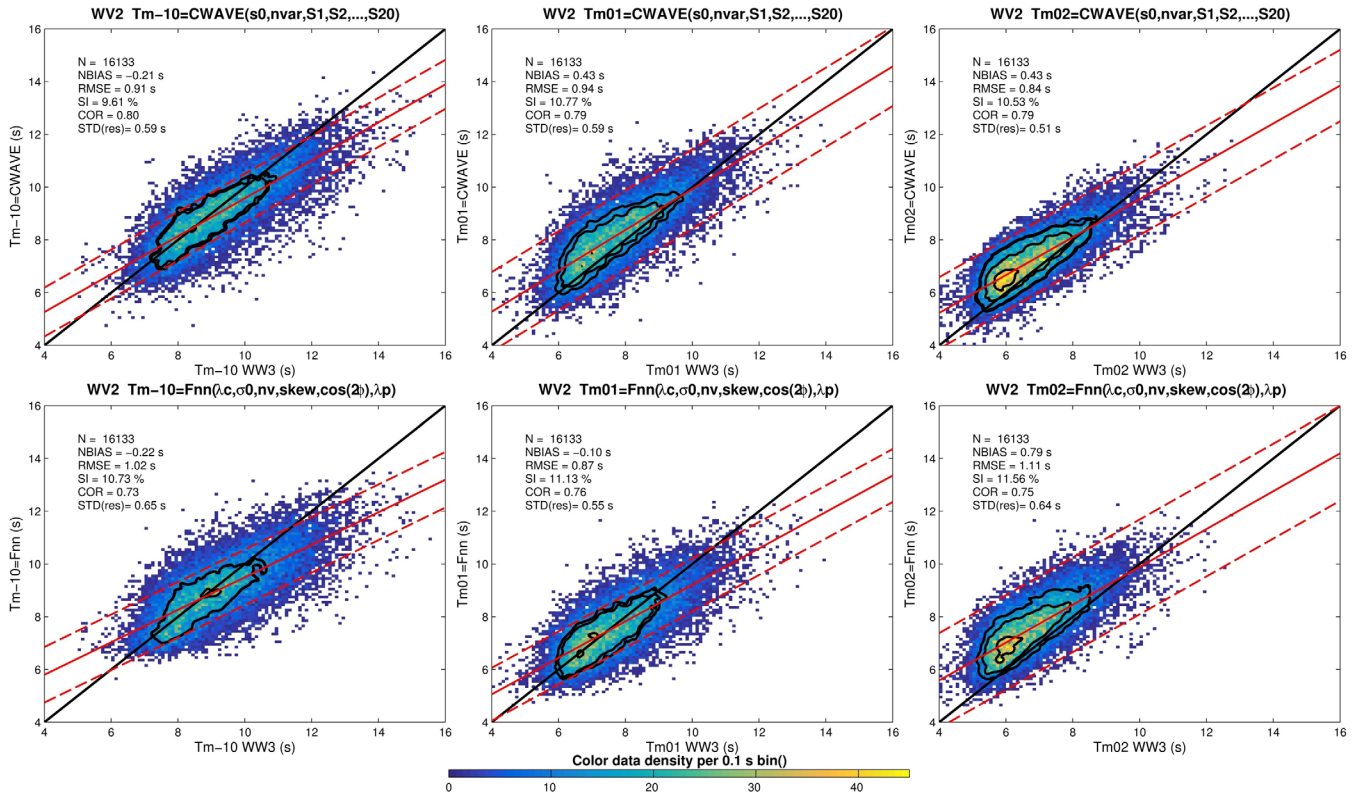


**Figure C2.** Average wave period comparison for September 2015 for WV2. (top) CWAVE and (bottom)  $F_{nn}$  for three different average wave periods. The color represents the data density in 0.1 s bins, solid red line represents a least square linear regression, and the dashed lines represent 90% of the data.

$$\bar{h}_{ij}(\alpha_k, \alpha_\phi) = \eta(k_x, k_y) g_i(\alpha_k) f_j(\alpha_\phi), \quad 1 \leq i \leq n_k; 1 \leq j \leq n_\phi \quad (B3)$$

where  $\eta$  is the elliptic area. The four Gegenbauer polynomials are

$$g_1(\alpha_k) = \frac{1}{2} \sqrt{3} \sqrt{1 - \alpha_k^2} \quad (B4)$$

$$g_2(\alpha_k) = \frac{1}{2} \sqrt{15} \alpha_k \sqrt{1 - \alpha_k^2} \quad (B5)$$

$$g_3(\alpha_k) = \frac{1}{4} \sqrt{\frac{7}{6}} (15\alpha_k^2 - 3) \sqrt{1 - \alpha_k^2} \quad (B6)$$

$$g_4(\alpha_k) = \frac{1}{4} \sqrt{\frac{9}{10}} (35\alpha_k^3 - 15\alpha_k^2) \sqrt{1 - \alpha_k^2}. \quad (B7)$$

The five harmonic functions are

$$f_1(\alpha_\phi) = \sqrt{1/\pi} \quad (B8)$$

$$f_2(\alpha_\phi) = \sqrt{2/\pi} \sin(2\alpha_\phi) \quad (B9)$$

$$f_3(\alpha_\phi) = \sqrt{2/\pi} \cos(2\alpha_\phi) \quad (B10)$$

$$f_4(\alpha_\phi) = \sqrt{2/\pi} \sin(4\alpha_\phi) \quad (B11)$$

$$f_5(\alpha_\phi) = \sqrt{2/\pi} \cos(4\alpha_\phi). \quad (B12)$$

Finally the integration area in the wavenumber domain have an elliptic shape in the SAR azimuth direction

$$\alpha_k(k_x, k_y) = 2 \frac{\log\left(\sqrt{a_1 k_x^4 + a_2 k_y^2 + k_y^2}\right) - \log(k_{\min})}{\log(k_{\max}) - \log(k_{\min})} - 1 \quad (B13)$$

$$\alpha_\phi(k_x, k_y) = \arctan(k_y, k_x) \quad (B14)$$

where the parameters  $a_1$  and  $a_2$  are defined as

$$a_1 = \frac{\gamma^2 - \gamma^4}{\gamma^2 k_{\min}^2 - k_{\max}^2} \quad (B15)$$

$$a_2 = \frac{k_{\max}^2 - \gamma^4 k_{\min}^2}{k_{\max}^2 - \gamma^2 k_{\min}^2} \quad (B16)$$

The values for  $k_{\max}$ ,  $k_{\min}$ , and  $\gamma$  are

$$k_{\max} = \frac{2\pi}{60m} \quad (B17)$$

$$k_{\min} = \frac{2\pi}{625m} \quad (B18)$$

$$\gamma = 2. \quad (B19)$$

For a more detailed description refer to Schulz-Stellenfleh et al. [2007] and Li et al. [2011] who used the same orthogonal functions.

### Appendix C: Average Wave Period Retrievals

In addition, to developing models to predict  $H_s$ , we also estimated average wave periods. There are various definitions of the average wave period and we use

$$Tm-10 = \frac{m_{-1}}{m_0} \quad (C1)$$

$$Tm01 = \frac{m_0}{m_1} \quad (C2)$$

$$Tm02 = \frac{m_0}{m_2} \quad (C3)$$

where  $m_n$  is a moment of the wave spectrum F

$$m_n = \int_0^\infty (2\pi f)^n F(f) df. \quad (C4)$$

We implement same training procedure described in the main text. We compare the month of September 2015 that was not used in the training for validation in Appendix Figures Figure C1 and Figure C2 for WV1 and WV2, respectively. In general there is a large error dispersion. We relate some of this to the fact that two very different sea states can have the same wave period. Both approaches are able to estimate the average wave period with accuracy and RMSEs are usually less than 1 s. However, the SIs are mostly less than 10%. This is a topic of future research.

### References

- Alpers, W. R., D. B. Ross, and C. L. Rufenach (1981), On the detectability of ocean surface waves by real and synthetic aperture radar, *J. Geophys. Res.*, *86*(C7), 6481–6498, doi:10.1029/jc086ic07p06481.
- Aouf, L., and J.-M. Lefevre (2015), On the impact of the assimilation of SARAL/AltiKa wave data in the operational wave model MFWAM, *Mar. Geod.*, *38*, suppl. 1, 381–395, doi:10.1080/01490419.2014.1001050.
- Arduin, F., B. Chapron, and F. Collard (2009), Observation of swell dissipation across oceans, *Geophys. Res. Lett.*, *36*, L06607, doi:10.1029/2008GL037030.
- Arduin, F., et al. (2010), Semiempirical dissipation source functions for ocean waves. Part I: Definition, calibration, and validation, *J. Phys. Oceanogr.*, *40*(9), 1917–1941, doi:10.1175/2010JPO4324.1.
- Beal, R. C., D. G. Tilley, and F. M. Monaldo (1983), Large- and small-scale spatial evolution of digitally processed ocean wave spectra from SEASAT synthetic aperture radar, *J. Geophys. Res.*, *88*(C3), 1761–1778, doi:10.1029/jc088ic03p01761.

### Acknowledgments

This paper has been possible thanks to SAR data access granted by ESA projects: Sentinel-1 A Mission Performance Center (4000107360/12/-LG) and Sentinel-1 Ocean Study (S1-4SCI-16-0002). All Sentinel L2 data used in this study can be obtained from the Copernicus Data Hub (cophub.copernicus.eu). ECMWF forecast winds were obtained in the framework of Sentinel-1 A Mission Performance Center (4000107360/12/-LG) ESA project. ECMWF forecast winds are publicly available (ecmwf.int). The altimeter wave data can be obtained from globwave.ifremer.fr. The buoy data can be obtained from the respective centers: NDBC (nodc.noaa.gov/BUOY/), MEDS (.meds-sdmm.dfo-mpo.gc.ca), and CDIP (cdip.ucsd.edu). We would like to thank the two anonymous reviewers for their comments which improved the paper.

- Bruck, M., and S. Lehner (2015), TerraSAR-X/TanDEM-X sea state measurements using the XWAVE algorithm, *Int. J. Remote Sens.*, *36*(15), 3890–3912, doi:10.1080/01431161.2015.1051630.
- Chapron, B., H. Johnsen, and R. Garello (2001), Wave and wind retrieval from SAR images of the ocean, *Ann. Telecommun.*, *56*(11), 682–699, doi:10.1007/BF02995562.
- Collard, F., F. Ardhuin, and B. Chapron (2005), Extraction of coastal ocean wave fields from SAR images, *IEEE J. Oceanic Eng.*, *30*(3), 526–533, doi:10.1109/JOE.2005.857503.
- Collard, F., F. Ardhuin, and B. Chapron (2009), Monitoring and analysis of ocean swell fields from space: New methods for routine observations, *J. Geophys. Res.*, *114*, C07023, doi:10.1029/2008JC005215.
- Engen, G., and H. Johnsen (1995), SAR-ocean wave inversion using image cross spectra, *IEEE Trans. Geosci. Remote Sens.*, *33*(4), 1047–1056, doi:10.1109/36.406690.
- Gourrion, J., D. Vandemark, S. Bailey, B. Chapron, G. P. Gommenginger, P. G. Challenor, and M. A. Srokosz (2002), A two-parameter wind speed algorithm for ku-band altimeters, *J. Atmos. Oceanic Technol.*, *19*(12), 2030–2048, doi:10.1175/1520-0426(2002)019<2030:ATPW-SA>2.0.CO;2.
- Grieco, G., W. Lin, M. Migliaccio, F. Nirchio, and M. Portabella (2016), Dependency of the sentinel-1 azimuth wavelength cut-off on significant wave height and wind speed, *Int. J. Remote Sens.*, *27*(21), 5086–5104, doi:10.1080/01431161.2016.1226525.
- Hagan, M. T., H. B. Demuth, M. H. Beale, and O. D. Jesus (2014), *Neural Network Design*, 2nd ed., Martin Hagan, Oklahoma State University.
- Hasselmann, K., and S. Hasselmann (1991), On the nonlinear mapping of an ocean wave spectrum into a synthetic aperture radar image spectrum and its inversion, *J. Geophys. Res.*, *96*(C6), 10,713–10,729, doi:10.1029/91JC00302.
- Hasselmann, K., R. K. Raney, W. J. Plant, W. Alpers, R. A. Shuchman, D. R. Lyzenga, C. L. Rufenach, and M. J. Tucker (1985), Theory of synthetic aperture radar ocean imaging: A Marsen view, *J. Geophys. Res.*, *90*(C3), 4659–4686, doi:10.1029/jc090ic03p04659.
- Hasselmann, S., C. Bruning, K. Hasselmann, and P. Heimbach (1996), An improved algorithm for the retrieval of ocean wave spectra from synthetic aperture radar image spectra, *J. Geophys. Res.*, *101*(C7), 16,615–16,629, doi:10.1029/96JC00798.
- Kerbaol, V., B. Chapron, and P. W. Vachon (1998), Analysis of ers-1/2 synthetic aperture radar wave mode images, *J. Geophys. Res.*, *103*(C4), 7833–7846, doi:10.1029/97JC01579.
- Krogstad, H. E., O. Samset, and P. W. Vachon (1994), Generalizations of the nonlinear ocean-SAR transform and a simplified SAR inversion algorithm, *Atmos. Ocean*, *32*(1), 61–82, doi:10.1080/07055900.1994.9649490.
- Li, X.-M. (2016), A new insight from space into swell propagation and crossing in the global oceans, *Geophys. Res. Lett.*, *43*, 5202–5209, doi:10.1002/2016GL068702.
- Li, X.-M., S. Lehner, and T. Bruns (2011), Ocean wave integral parameter measurements using ENVISAT ASAR wave mode data, *IEEE Trans. Geosci. Remote Sens.*, *49*(1), 155–174, doi:10.1109/TGRS.2010.2052364.
- Mouche, A., and B. Chapron (2015), Global c-band ENVISAT, RADARSAT-2 and sentinel-1 SAR measurements in copolarization and cross-polarization, *J. Geophys. Res. Oceans*, *120*, 7195–7207, doi:10.1002/2015JC011149.
- Mouche, A. A., F. Collard, B. Chapron, K.-F. Dagestad, G. Guitton, J. A. Johannessen, V. Kerbaol, and M. W. Hansen (2012), On the use of Doppler shift for sea surface wind retrieval from SAR, *IEEE Trans. Geosci. Remote Sens.*, *50*(7), 2901–2909, doi:10.1109/TGRS.2011.2174998.
- Queffeuilou, P., and D. Croize-Fillon (2016), Global altimeter SWH data set, *Tech. Rep. 11.2*, Institut francais de recherche pour l'exploitation de la mer (IFREMER)/Centre ERS d'Archivage et de Traitement (CERSAT), Plouzane, France.
- Quilfen, Y., B. Chapron, A. Bentamy, J. Gourrion, T. El Fouhaily, and D. Vandemark (1999), Global ERS 1 and 2 and NSCAT observations: Upwind/crosswind and upwind/downwind measurements, *J. Geophys. Res.*, *104*(C5), 11,459–11,469, doi:10.1029/1998JC900113.
- Rascole, N., and F. Ardhuin (2013), A global wave parameter database for geophysical applications. Part 2: Model validation with improved source term parameterization, *Ocean Modell.*, *70*, 174–188, doi:10.1016/j.ocemod.2012.12.001.
- Reul, N., B. Chapron, E. Zabolotskikh, C. Donlon, Y. Quilfen, S. Guimbard, and J. Piolle (2016), A revised I-band radio-brightness sensitivity to extreme winds under tropical cyclones: The five year SMOS-storm database, *Remote Sens. Environ.*, *180*, 274–291, doi:10.1016/j.rse.2016.03.011.
- Romeiser, R., H. C. Graber, M. J. Caruso, R. E. Jensen, D. T. Walker, and A. T. Cox (2015), A new approach to ocean wave parameter estimates from c-band scan-SAR images, *IEEE Trans. Geosci. Remote Sens.*, *53*(3), 1320–1345, doi:10.1109/TGRS.2014.2337663.
- Schulz-Stellenfleth, J. (2005), A parametric scheme for the retrieval of two-dimensional ocean wave spectra from synthetic aperture radar look cross spectra, *J. Geophys. Res.*, *110*, C05004, doi:10.1029/2004JC002822.
- Schulz-Stellenfleth, J., T. Knig, and S. Lehner (2007), An empirical approach for the retrieval of integral ocean wave parameters from synthetic aperture radar data, *J. Geophys. Res.*, *112*, C03019, doi:10.1029/2006JC003970.
- Sepulveda, H. H., P. Queffeuilou, and F. Ardhuin (2015), Assessment of SARAL/AltiKa wave height measurements relative to buoy, Jason-2, and Cryosat-2 data, *Mar. Geod.*, *38* suppl. 1, 449–465, doi:10.1080/01490419.2014.1000470.
- Shao, W., Z. Zhang, X. Li, and H. Li (2016), Ocean wave parameters retrieval from sentinel-1 SAR imagery, *Remote Sens.*, *9*(9), 707–721, doi:10.3390/rs8090707.
- Stoffelen, A., and D. Anderson (1997), Scatterometer data interpretation: Estimation and validation of the transfer function cm04, *J. Geophys. Res.*, *102*(C3), 5767–5780, doi:10.1029/96JC02860.
- Stopa, J. E., and K. F. Cheung (2014), Intercomparison of wind and wave data from the ECMWF reanalysis interim and the NCEP climate forecast system reanalysis, *Ocean Modell.*, *75*, 65–83, doi:10.1016/j.ocemod.2013.12.006.
- Stopa, J. E., K. F. Cheung, H. L. Tolman, and A. Chawla (2013), Patterns and cycles in the climate forecast system reanalysis wind and wave data, *Ocean Modell.*, *70*, 207–220, doi:10.1016/j.ocemod.2012.10.005.
- Stopa, J. E., F. Ardhuin, A. Babanin, and S. Zieger (2015a), Comparison and validation of physical wave parameterizations in spectral wave models, *Ocean Modell.*, *103*(7), 2–17, doi:10.1016/j.ocemod.2015.09.003.
- Stopa, J. E., F. Ardhuin, B. Chapron, and F. Collard (2015b), Estimating wave orbital velocity through the azimuth cutoff from space-borne satellites, *J. Geophys. Res. Oceans*, *120*, 7616–7634, doi:10.1002/2015JC011275.
- Stopa, J. E., F. Ardhuin, R. Husson, H. Jiang, B. Chapron, and F. Collard (2016), Swell dissipation from 10 years of ENVISAT advanced synthetic aperture radar in wave mode, *Geophys. Res. Lett.*, *43*, 3423–3430, doi:10.1002/2015GL067566.
- Vachon, P. W., H. E. Krogstad, and J. S. Paterson (1994), Airborne and space-borne synthetic aperture radar observations of ocean waves, *Atmos. Ocean*, *32*(1), 83–112, doi:10.1080/07055900.1994.9649491.
- Zabolotskikh, E. V., N. Reul, and B. Chapron (2016), Geophysical model function for the AMsr2 C-band wind excess emissivity at high winds, *IEEE Geosci. Remote Sens. Lett.*, *13*(1), 78–81, doi:10.1109/LGRS.2015.2497463.